Knapmeyer, M., Knapmeyer-Endrun, B., Plesa, A., Bose, M., Kawamura, T., Clinton, JF., Golombek, MP., Kedar, S., Stahler, S., Stevanovic, J., Perrin, C., Lognonne, P., Teanby, N., & Weber, R. (2019). Estimation of the Seismic Moment Rate from an Incomplete Seismicity Catalog, in the Context of the InSight Mission to Mars. *Bulletin of the Seismological Society of America*. https://doi.org/10.1785/0120180258

Peer reviewed version

Link to published version (if available):
10.1785/0120180258

Estimation of the seismic moment rate from an incomplete seismicity catalog, in the context of the InSight mission to Mars

M. Knapmeyer

B. Knapmeyer-Endrun

A.-C. Plesa

M. Böse

T. Kawamura

J.F. Clinton

M.P. Golombek

S. Kedar

S. Stähler

J. Stevanović

C. Perrin

P. Lognonné

N.A. Teanby

R.C. Weber

Corresponding Author:

Martin Knapmeyer

DLR Institute for Planetary Research

Rutherfordstr. 2

12489 Berlin

martin.knapmeyer@dlr.de

phone: 0049-30-67055394

Abstract

We evaluate methods to estimate the global seismic moment rate of a planet from the $k \geq 1$ largest events observed during a limited and possibly short time span, as can be expected e.g. for lander missions to Mars. The feasibility of the approach is demonstrated with a temporary broadband seismometer that was recording in the Mojave Desert, California, for 86 days in 2014, and by application to the Global Centroid Moment Tensor catalog, subsets thereof, and a catalog of stable continental regions seismicity . From the largest event observed at Goldstone alone ($M_W \approx 7.9$) we estimate the Earth's global moment rate to be $1.03 \times 10^{22}\ Nm/yr$, while an estimation based on the 10 strongest events yields a rate of $5.79 \times 10^{21}\ Nm/yr$. Summation of 42 years of GCMT solutions result in an average of $7.61 \times 10^{21}\ Nm/yr$. In general, a two years interval of GCMT solutions is sufficient to estimate the Earth's annual moment rate to within a factor 5 or better. A series of numerical experiments with more than 560 million synthetic catalogs based on the Tapered Gutenberg-Richter distribution shows that the estimation is rather insensitive against an unknown slope of the distribution, and that bias and variance of the estimator depend on the ratio between moment rate and corner moment of the size frequency distribution. Moment rates of published Mars models differ by a factor 1000 or more. Tests with simulated catalogs show that it will be possible to reject some of these models with data returned by NASA's InSight mission after two years of nominal mission life time.

Introduction

The InSight mission (Banerdt et al., 2013) to Mars was launched on May 5, 2018 from Vandenberg Air Force Base, California, and touched down softly in the targeted landing ellipse on Elysium Planitia, Mars, on November 26, 2018. A combined very broad band and short period seismometer was deployed on the surface on 19th of December 2018 and is intended to operate until the end of 2020 (Lognonné & Pike, 2015, Lognonné et al., submitted).

Models for the seismicity of planet Mars usually estimate the long-term average annual seismic moment rate (Table 1), and also the average annual event rate. This holds for estimations based on geological evidence (Golombek et al., 1992, Golombek, 2002, Taylor et al., 2013) as well as for models based on thermal evolution and cooling of the Martian lithosphere (Phillips, 1991, Knapmeyer et al., 2006, Plesa et al., 2018). All studies are compatible with the conclusion drawn from the non-observation of any unambiguous seismic event by the Viking missions (Anderson et al., 1977, Goins & Lazarewicz, 1979), i.e. that Martian seismicity ranges somewhere between that of the Moon and that of Earth. However the range of predicted moment rates is wide and observational constraints of moment rate are therefore desirable to reject models and further our understanding of planetary heat engines. Here we investigate to what extent the InSight mission can be expected to contribute to the rejection of seismicity models. The main obstacles are that the detection threshold of a single station will be relatively high compared to a global network, while the expected life time is relatively short compared to the instrumental record available for Earth. Our approach basically relies on most of the seismic moment being released in a few, large events, and employs Monte Carlo methods to assess how likely any given seismicity model results in the moment rate estimation obtained from the recorded marsquakes.

Statistical seismology on celestial bodies other than Earth generally suffers from limitations in the life time and station spacing of seismic networks: On the Moon, the first long period seismometer was de-

ployed in 1969, later augmented by four more stations to form a triangle (Apollo 12 and 14 were relatively close together, compared with Apollo 15 and 16). The network was shut down in late 1977 (Vostreys, 1980). One seismometer (Viking 2) was in operation on Mars from September 1976 to April 1978, i.e. for about 20 months (Toksöz, 1979). The Venera 13 and 14 missions each landed one seismometer on Venus on the 1st of March 1982 (Venera 13) and 3rd of March 1982 (Venera 14), respectively, and with lander life times of 127 and 57 minutes (Siddiqi, 2002). During these times, about 1.5 minutes of seismic waveforms and, additionally, statistical waveform parameters derived on board, were downlinked to Earth (Ksanfomaliti et al., 1982). The Huygens probe contained a suite of accelerometers to monitor its path through the atmosphere of Titan and to record the touchdown shock. Although not intended to conduct a surface seismic experiment, the HASI accelerometer onboard the Huygens probe continued to record data for approximately 30 min after touchdown (Hathi et al., 2009). A network of three triaxial accelerometers was deployed on comet 67P/Churuyomov-Gerasimenko within the landing gear of Rosetta's lander Philae, resulting in a network aperture of about 2.5 m (Knapmeyer et al., 2016). From this experiment, about 70 s of high-frequency data (sampling rates up to 16 kHz) were returned. With a design life time of two terrestrial years, InSight will significantly surpass these recent experiments.

An instructive comparison to the much better coverage of the Earth arises from the Global Centroid Moment Tensor project (GCMT, Dziewonski et al., 1981, Ekström et al., 2012). At the same time the first seismometers were launched to Mars, the GCMT started producing its catalog of Earthquake source mechanisms, complete to magnitudes of about five and currently based on data from nearly 200 seismic observatories distributed worldwide. The GCMT continuously contributed to the picture of Earth's moment-frequency distribution for the whole 42 years during which there was not even a single seismometer on Mars.

Besides the relatively short period of time covered by extraterrestrial seismicity catalogs so far, spatial coverage and completeness thresholds result in additional obstacles for the estimation of distribu-

tion parameters. Even within the Apollo network on the Moon, the most extensive network outside Earth so far, distance between stations was around 30°, i.e. the network triangle covered only a small fraction of the lunar surface. Limited spatial coverage results in a distance dependent detection threshold: small events will be detected only in the vicinity of the network or station, if there is but one. In turn, large, globally detectable events will be overrepresented in the catalog such that the moment-frequency distribution appears to be less steep than it actually is. Also, the estimation of event rates must rely on assumptions about source distribution in distant areas in order to extrapolate the detected local or regional seismicity to the entire planet.

The seismic moment of Earthquakes is predominantly released by the few largest events. This suggests that it is possible to obtain a reasonable estimate of the seismic moment rate from evaluating only a small number of large events, or even from the single largest event ever observed. Central questions are how such an estimate can be obtained and how accurate it will be, and also what accuracy is necessary to make a rate estimation a useful constraint to improve our understanding of Mars.

To answer the latter, we consider the moment rate estimates summarized in Table 1. Moment rates given there for Earth and Moon differ by almost exactly ten orders of magnitude, or 4.7 moment magnitude units. The individual estimations for Mars cover a range of 2.1 moment magnitude units, or a factor of approximately 1150 in the seismic moment. It is thus desirable to estimate the moment rate with accuracy better than this in order to reject some or several of the published seismicity models.

In the following, we will first describe our proposed approaches for moment rate estimation, and how we generate synthetic seismicity catalogs for numerical testing (section "Methods"). The available catalogs are described in section "Data". Since no event catalog is currently available for Mars, we briefly summarize the seismotectonic background information available for Mars. To test if reasonable results can be obtained, we evaluate several seismicity catalogs for the Earth, discuss the applicability to the Moon, and evaluate synthetic catalogs in a generic parameter study and for Mars-specific models (sec-

tion “Results”). Section "Single Station Completeness Threshold" specifically demonstrates that a single broadband station is sufficient to obtain a meaningful moment rate estimate for an entire planet within a relatively short time.

Methods

As Kagan & Schoenberg (2001) point out, a statistical consideration of magnitudes rather than moments is advantageous by transforming multiplicative uncertainties into additive ones. Besides, taking the logarithm of the moment transforms the numerical values in to a more convenient range.

Throughout this work, we will frequently convert seismic moments M into equivalent moment magnitudes m via

$$m = \frac{2}{3}(log_{10}M - 9.1) \quad (1)$$

(after Bormann et al., 2002). Using this formula, we also express moment rates as if the entire moment was released in a single event. All magnitudes used throughout this paper are moment magnitudes following from the above equation, unless indicated otherwise. The coefficient $2/3$ implies that a factor of 1000 in the moment M corresponds to a difference of exactly 2 moment magnitude units. We denote seismic moments by uppercase letters and magnitudes by lowercase letters to avoid the excessive indexing that would result from the conventional lettering, and two indexed quantities M_x and m_x refer to moments and magnitudes connected by the above equation.

The coefficients of eq. 1 originate in a calibration of the seismic moment scale to other magnitude scales and thus carry a certain heritage of Earth’s seismological properties, e.g. via the decay of surface waves over distances not available e.g. on Mars. It must be kept in mind that relations to seismogram

amplitudes and, moreover, intensities will differ between Earth, Mars, and other bodies. Appropriate magnitude scales for Mars have been developed by Böse et al. (2018).

Seismic Moment Rate Estimation

Following the seminal works by Gutenberg & Richter (1941, 1944), the size-frequency distribution of earthquakes is often described by what we now call a power law, although Gutenberg & Richter were aware that the frequency of very large events cannot follow the same law as the frequencies of small and medium ones for physical reasons. Assuming a fault plane as large as the Earth's surface, and with a slip proportional to the square root of the fault area as in the relations given in Knapmeyer et al. (2006), we find a resulting seismic moment of $7 \times 10^{28}\ Nm$ (corresponding to $m = 13.2$) being a hard upper limit for quake size on Earth, as any geologically plausible fault would have a smaller rupture area. The extrapolation of the linear part of the size-frequency distribution of the GCMT predicts that events of this size occur every 10000 to 100000 years: The classical Gutenberg-Richter law, when interpreted naively, predicts that ridiculously large events recur on time scales that are short compared to e.g. the Wilson cycle. Given that there are no traces at all of such events, we take it as an observational fact that this prediction is not true and the size-frequency distribution must bend down significantly somewhere between $5.3 \times 10^{22}\ Nm$ (the Tohoku event of March 2011) and $10^{29}\ Nm$.

We assume that the moment frequency distribution follows a tapered Pareto distribution (a.k.a. tapered Gutenberg-Richter distribution), which basically is a Gutenberg-Richter law tapered with an exponential function for the largest events (Figure 1).

In this distribution, the cumulative relative number of events with a seismic moment larger than M is given by (Kagan, 2002a, b, and references therein)

$$\Phi(\mathrm{M}) = \left(\frac{M_t}{M}\right)^{\beta} exp\left(\frac{M_t - M}{M_c}\right) \text{ for } M_t \leq M < \infty \quad (2)$$

Here M_c is the "corner moment" where the exponential taper gains dominance over the classical Gutenberg-Richter power law relation, M_t is the threshold moment above which the catalog is complete (not to be confused with the detection threshold M_d, i.e. the smallest moment for which the catalog contains some, but not all, events), and β is a slope parameter. The part of the graph of Figure 1 for $M_d \leq M \leq M_t$, i.e. the incomplete detection of events between detection threshold M_d and completeness threshold M_t, is not described by eq. 2 as it is at least partially controlled by effects and properties not related to the quake production, like background noise, anelasticity, and instrument sensitivity.

To obtain absolute numbers, $\Phi(M)$ has to be multiplied with a calibration factor following Kagan (2002b)

$$\alpha_0 = \frac{\dot{M}_S M_c^{\beta}(1-\beta)}{M_t^{\beta} M_c \Gamma(2-\beta) exp(M_t/M_c)} \qquad (3)$$

where $\dot{M}_S$ is the moment release rate per unit time of events exceeding M_t, and $\Gamma(x)$ is the Gamma function with $\sqrt{\pi/4} \leq \Gamma(2-\beta) \leq 1$ for $0.5 \leq \beta \leq 1$ (e.g. Weisstein, undated). The absolute rate $\dot{N}(M)$ of events with a seismic moment larger than M is thus obtained from combining eqs. 2 and 3

$$\dot{N}(M) = \alpha_0 \Phi(M) \qquad (4)$$

In addition to the rate $\dot{M}_S$ we introduce the cumulative moment M_S such that one event of size M_S per unit time would account for the entire moment rate.

If the completeness threshold can be made small enough, $M_t \ll M_c$, the exponential term approaches one and $\dot{N}(M) \propto \dot{M}_S M_c^{\beta-1}$, which plots as a straight line in log-log coordinates, such that the observed event rate allows inferences on $\dot{M}_S M_c^{\beta-1}$.

For any catalog of observed events, one can estimate $\dot{N}(M)$ via the number N of events listed in the catalog (not taking into account those below M_t), and the time span covered by it.The moment rate can be estimated by summing up all events and dividing by the number of unit time intervals covered by the catalog, as was done with the GCMT in Table 1.

The total moment released can be computed by integration over the distribution, but since the moment rate is a factor in $\dot{N}(M)$ we can save the integration and solve $\dot{N}(M)$ for $\dot{M}_S$

$$\dot{M}_S = \dot{N}(M)\frac{\Gamma(2-\beta)}{1-\beta}\frac{M^\beta}{M_c^{\beta-1}}exp\left(\frac{M}{M_c}\right) \qquad (5)$$

Although M_t cancelled out, $\dot{M}_S$ is still only the moment rate resulting from events exceeding M_t by implication via $\dot{N}$. If $M_t \ll M_c$ and $\beta < 1$, the difference to the moment rate resulting from all events is however neglible.

Now we consider only the largest event that ever occurred. By definition, the largest event ever (or LVR, for short, from *L*argest e*V*ent eve*R*) is contained in the catalog only once. Thus, if the catalog covers a time interval of n unit intervals, we identify $M = M_{LVR}$ and obtain $\dot{N}(M_{LVR}) = 1/n$, and eq. 5 allows estimating the global moment rate from a single event, provided the corner moment M_c of the distribution and its slope parameter, or reasonable estimates, are given.

Using eq. 2 we find the relative frequencies of events exceeding M_c by a factor x is

$$\frac{\Phi(xM_c)}{\Phi(M_c)} = \left(\frac{1}{x}\right)^\beta exp(1-x) \qquad (6)$$

With a convenient (and not entirely unrealistic) value of $\beta = 2/3$, this results in a drop of frequency by a factor 5×10^{-15} for events one magnitude unit larger than m_c, while the frequency of events two magnitude units larger is reduced by 10^{436} with respect to the corner moment. Thus the former are

extremely rare, while the latter do practically not occur. This holds for slightly different choices of β as well.

The largest event ever hence poses a (statistical) lower limit $M_{LVR} \leq M_c$ simply by its existence. Moreover, it will approach the corner moment with time, such that $M_{LVR} \approx M_C$ becomes a reasonable guess. Inserting this into eq. 5 yields

$$M_S \approx \frac{1}{n}\frac{\Gamma(2-\beta)}{1-\beta} M_{LVR} \qquad (7)$$

and we call this the normalized largest event ever, NLVR for short, estimation of the moment rate.

The middle term approaches infinity for $\beta \to 1$, but in reality $1/2 \leq \beta \leq 2/3$ appears to hold, from which $\sqrt{\pi} \leq \Gamma(2-\beta)/(1-\beta) \leq 2.68$ follows.

We define n based on the duration of the observation: if the unit time interval has a duration ΔT, seismicity is recorded between t_{start} and t_{end} (where t_{start} is not necessarily the time of the first event, and t_{end} is continuously growing in an ongoing experiment), then the normalization factor for the largest event ever which occurred at a time t_{LVR} between start and end is $n = (t_{end} - t_{start} + 1)/\Delta T$, and also continuously grows in an ongoing experiment.

With this definition, $1/n$ and thus the estimated value of $\dot{M}_S$, will approach zero for $t_{end} \to \infty$. Mathematically, this appears to be a flaw, but in the long run the observer can take the onset of a continuous decay as indication that the largest event ever has exceeded the corner moment of the distribution.

A more sophisticated estimation of M_c is given by Kagan & Schoenberg (2001). As they found that a maximum likelihood estimation of M_c is severely biased for small catalogs, they derive an alternate estimator based on expressions for the first and second statistical moment of the tapered Gutenberg-Richter distribution. With the seismic moment of the i-th event in the catalog termed M_i, a total of k cataloged events, the standard deviation σ of the M_i, and the mean moment

$$\bar{M} = \frac{1}{k}\sum_{i=1}^{k} M_i \qquad (8)$$

they obtain the estimator

$$\widetilde{M}_c = \frac{\sum(M_i^2/k) - M_t^2}{2\left[M_t^2\beta + (1-\beta)\bar{M}\right]} \qquad (9)$$

from which a bias correction

$$\widetilde{M}_{bias} = \frac{(\beta-1)\left[2M_t^3 + 3M_t^2\widetilde{M}_c\beta + \left(\sigma^2+\bar{M}^2\right)(6\widetilde{M}_c - 3\widetilde{M}_c\beta - 2\bar{M})\right]}{4k[M_t\beta + (1-\beta)\bar{M}]^2} \qquad (10)$$

has to be subtracted. The difference $\widetilde{M}_c - \widetilde{M}_{bias}$ is then substituted for M_c in eq. 5.

The estimator $\widetilde{M}_c - \widetilde{M}_{bias}$ holds for i.i.d. events, i.e. the parameters of the earthquake-generating distribution must be constant in time, and the quakes must not trigger each other. Therefore the catalog has to be declustered before estimating the corner moment. We call the combination of equations 5, 9, and 10 the k-events Kagan-Schoenberg, or KS_k for short, estimator of the moment rate.

The KS_k estimator requires a catalog containing at least k events and a reasonable estimate about the completeness threshold M_t of that catalog to be computable and useful. If only a single event is available, one can either equate M_t with the size of that event, resulting in $\widetilde{M}_c = 0$, or assume that M_t is smaller than the event, resulting in $\widetilde{M}_c$ being dependent only on that assumption but not on the observed event. Moreover, σ and hence $\widetilde{M}_{bias}$ are undefined for a single event. Therefore the KS_k estimator cannot be used with a single event.

The event magnitudes or seismic moments in a real marsquake catalog will carry an uncertainty as discussed by Böse et al. (2018). This uncertainty for individual events is propagated into the uncertainty of NLVR and KS_k estimations in a Monte Carlo fashion by evaluating a number of modified catalogs, where each event's seismic moment is perturbed according to a normal distribution with the standard

239 deviation cataloged for this individual event, and taking care for error propagation through conversion
240 between different types of magnitudes or magnitudes and seismic moments.

241 Emission Probabilities

242 Due to the stochastic nature of the tectonic process generating the real quakes, as well as of any cata-
243 log simulation process, simulated catalogs will never match observed quake sequences on an event-by-
244 event basis even if the model underlying the simulation matches the real process perfectly, and all pa-
245 rameters are known exactly.

246 Due to the limitations of the data set we expect to obtain for Mars, we do not consider a maximum-
247 likelihood fit of an assumed type of distribution in order to estimate its parameters feasible.

248 The moment rate estimation described above is intended to be a direct estimation of one of the pa-
249 rameters of the size-frequency distribution, but is likely to be biased and carry some variance, not the
250 least due to the uncertainty of the seismic moments of observed events. Bias and variance will depend
251 on several factors, such as the parameters of the Tapered Gutenberg-Richter distribution themselves,
252 and the period of time covered by the simulated catalog.

253 We borrow (without intending to over-stress the analogy) from the field of hidden layer Markov
254 chains the term "emission probability" for the probability that a stochastic process produces a statistical
255 diagnostic with the same value as obtained from another, inaccessible process: In our case, a quake cata-
256 log is a realization of a stochastic process which is transformed into a single-valued diagnostic using one
257 of our estimators. This transformation is a secondary stochastic process of which the resulting diagnostic
258 is a single realization. We aim to estimate the probability that a numerical simulation of seismicity cata-
259 logs results in the same moment rate estimations as the observed catalog.

260 The catalog simulation we describe in the next section is a random number generator with three pa-
261 rameters: moment rate, corner moment, and distribution slope. These parameters form a state space,

which we scan on a search grid with a regular node spacing when moment rate and corner moment are expressed as magnitudes following equation 1. For each node, we produce a large number of synthetic catalogs and evaluate the NLVR and KS_k estimators for all these catalogs, resulting in a distribution of estimations. Comparing these distributions with the respective estimations of the real catalog, we can determine the probability that a certain combination of state parameters makes the catalog simulation emit a moment rate estimation within the uncertainty limits of the moment rate estimation derived from the real catalog.

This finally yields a map of emission probabilities for the scanned part of the state space, which can then be compared with predicted parameters e.g. from Knapmeyer et al. (2006), or with values for Earth and Moon.

Examples will be shown below in sections dealing with seismicity catalogs for Earth and Moon, and synthetic catalogs for Mars. These are computed on a search grid with node spacing of 0.1 moment magnitudes in both moment rate and corner moment dimensions. For each grid node, we evaluate 1000 catalogs, resulting in 3.1 million catalogs for the depicted grids. We evaluate for each node the probability that a given state emits a value within 0.2 magnitude units (corresponding to a factor 2 in seismic moment) from the respective target values as given in figure titles (the GCMT comes without uncertainty ranges for the scalar moment, therefore we use a fixed interval width here). Computation time on a desktop computer fits into a lunch break and thus leaves room for refining the search grid or evaluating more catalogs per grid node.

Simulation of Seismicity Catalogs

Equation 2 only predicts the relative frequencies of events. In order to reproduce the seismicity observed during a time interval of duration Δt, it needs to be normalized in such a way that also the absolute number of events $N(M)$ and the observed cumulative moment $M_{cum} = \dot{M}\Delta t$ released by all events

in the catalog are reproduced. Following Kagan (2002b), the long term average α_0 is computed by evaluating eq. 3.

We adjust the – in our context entirely fictitious – completeness threshold M_t such that we obtain catalogs of approximately 10000 events.

The number $N_{\Delta t}$ of events in an actual time interval, e.g. a given calendar year, follows a Poisson distribution describing the probability that the value of $N_{\Delta t}$ is n (e.g. Zhuang et al., 2012)

$$P\{N_{\Delta t} = n\} = \frac{\lambda}{n!} e^{-\lambda} \quad (11)$$

where λ is the rate parameter of the distribution.

For a rate parameter exceeding about 10, the Poisson distribution can be approximated by a normal distribution with mean $\bar{x} = \lambda$ and standard deviation $\sigma = \sqrt{\lambda}$. For time intervals of the order of years and a sufficiently low detection threshold, one can expect hundreds or thousands of quakes, such that this condition is met. We thus draw the number of events per time interval from a normal distribution with $\lambda = \alpha_0$.

The distribution of earthquakes in time (when disregarding aftershocks) also follows a Poisson distribution, as was first shown for California by Gardner & Knopoff (1974). With the number n of events occurring during interval $\Delta\mathrm{T}$ already being given by eqs. 3 and 11, is it thus sufficient to distribute the source times uniformly over the time interval (see Zhuang & Touati, 2015, algorithm 10).

Finally, for each source time generated thus, a seismic moment is drawn from the tapered Pareto distribution, following the method described by Vere-Jones et al. (2001), which we reproduce here for self-containedness. We first generate a first set U_1 of n uniformly distributed random numbers from the interval $]0,1[$. From these we compute

$$y = U_1^{-1/\beta} \qquad (12)$$

In addition, we employ the inverse method to produce n exponentially distributed random numbers from a second set U_2 of n uniformly distributed random numbers which are then filtered through the inverse of the exponential distribution

$$X = -\frac{1}{\lambda} log(1 - U_2) \qquad (13)$$

to obtain a set X of exponentially distributed random numbers, where

$$\lambda = \frac{M+M_t}{M_c} \qquad (14)$$

is the rate parameter of the exponential distribution $f(\tau) = \lambda exp(-\lambda\tau)$. Finally,

$$K = (M + M_t) * \min(y, 1 + X) - M_t \qquad (15)$$

is a tapered Pareto distributed seismic moment value following the distribution given in eq. 2.

It should be noted that assuming a Poisson process is equivalent to the assumption that the individual events are entirely independent of each other, i.e. the process has no memory of the past. This assumption does not apply to foreshock/aftershock sequences, therefore a comparison of real catalogs with synthetic ones generated with the above procedure requires the declustering of the real catalog. Moreover, this kind of catalog simulation might be unsuitable for sources with a periodic driving force, such as deep moonquakes (DMQ).

It has been argued that the slope parameter β is actually not a free parameter but a universal constant with a value $\beta = 1/2$ (initially apparently by Vere-Jones, 1976, recently e.g. by Kagan, 2014). Analyses of different tectonic settings (Kagan, 1997), Flinn-Engdahl regions (Kagan, 1999) and rectangular regions defined by parallels and meridians (Godano & Pingue, 2000) support that β is a global constant

for quakes on Earth (except mid-oceanic ridges), however with a value $0.6 \leq \beta \leq 2/3$. Kagan (2014) argues that the deviation from the prediction is a combination of several observational biases.

Thermal moonquakes appear to follow a distribution where most of the moment is released by the small events (implying $\beta > 1$, Cooper & Kovach, 1975), and it is questionable that deep moonquakes, with a stress source that reverts direction on a monthly scale, fall under the same universal relation as subduction zone events resulting from a uniformly progressing slab. So although we follow Knapmeyer et al. (2006) that $\beta = 0.625$ is a good initial choice for Mars, lacking a better one for now, we are aware that this needs to be established experimentally, and it must not be taken for granted.

Data

The following subsections describe three seismicity catalogs for the Earth and one catalog for the Moon that were used as test cases for moment rate estimation. In the absence of a Mars seismicity catalog we give a brief summary of Martian seismotectonic properties that make us conclude that earthquake statistics methods based on terrestrial circumstances are applicable to Mars as well.

GCMT catalog

We downloaded the complete catalog of the Global Centroid Moment Tensor project (GCMT, Dziewonski et al., 1981, Ekström et al., 2012) from IRIS (see "Data and Resources"). This catalog covers the 15456 days from 05. January 1976 (date of the first event in the GCMT) to 17. May 2018, or 42.32 years of 365.25 days, and contains 49178 events with seismic moments between $3.49 \times 10^{15}\ Nm$ and $5.32 \times 10^{22}\ Nm$. The completeness threshold for the catalog as a whole is $M_t \approx 2 \times 10^{17}\ Nm$, but de-

creases with time; especially the year 1976 is significantly less complete, while M_t is lower for the more recent years.

The cataloged events released a cumulative seismic moment of $\sum M_0 = 3.23 \times 10^{23}\ Nm$. The ten largest events in this catalog released 47.5 % of $\sum M_0$, and the 615 largest events (i.e. 1.25 % of all events) released 90 % of $\sum M_0$.

Stable Continental Regions catalog

The Stable Continental Regions catalog of Schulte and Mooney (2005, see also "Data and Resources" represents a compilation for several sources of historically witnessed events and of events for which instrumental recordings exist, and covers the entire Earth for the time from 495 AD to 2003. Schulte and Mooney have estimated seismic moments for most of the 1373 events in the catalog. Cataloged moments range from $5.3 \times 10^{15}\ Nm$ to $7.5 \times 10^{23}\ Nm$, the latter however is assigned to a reservoir-associated event in India in September 2000 and is most likely erroneous. We exclude this and another reservoir-associated event for which a moment of $> 10^{23}\ Nm$ is given from our analysis, leaving as the largest listed event an earthquake that occurred in July 1819, also in India, with a seismic moment of $6.6 \times 10^{20}\ Nm$ ($M_w = 7.8$).

For each event, the catalog indicates if instrumental records, historical desriptions, or both are available. For events after 1976, the catalog is informed by the GCMT.

Temporary Installation at Goldstone, CA

A single Nanometrics Trillium Compact seismometer (120 *s* eigenperiod) was installed temporarily during summer 2014, in a dry lake bed in the Mojave desert, approximately 60 *km* NNE of Barstow, California, and approximately 1 *km* southwest of the 70 *m* “Mars” antenna dish of NASA’s Deep Space Network (Lorenz et al., 2015). The purpose of this experiment was to gather seismic and microbarometric

recordings of dust devils, to support the interpretation of dust devil recordings expected from Mars. The experiment was not intended to record earthquakes, but these are of course hard to avoid.

The surface of the lake bed is composed of fine mud that grades into denser sediment overlying a rock with increasing seismic velocities with depth, which is likely analogous to the InSight landing site (see Lorenz et al., 2015, Golombek et al., 2017, and Knapmeyer-Endrun et al., 2017). The seismometer was shallowly buried and accompanied by a microbarometer and an anemometer on the surface. The seismic sampling frequency was 100 *Hz*, but we resampled to 2 *Hz* to simulate the continuous data stream that will be available from InSight (Lognonné et al., submitted). The seismometer operated from 05. June 2014 to 29. Aug. 2014. Several downtime periods add up to 18 days (24h periods, not to be confused with the 24.6h of the martian rotation period) of lost data, such that a total of 68 days of seismic recordings remains.

During this experiment, the USGS National Earthquake Information Center (NEIC) catalog lists 304 global events with magnitudes of 5 and larger.

We convert the 7 different types of magnitudes found in the NEIC catalog (M_S, m_b, M_L, and several versions of M_W) into seismic moments to quantify source strength , using relations from Wason et al. (2012) , and from Bormann et al. (2002).

By visual inspection, we categorize all events according to their signal quality with categories given in Table 2. We expect that magnitudes or seismic moments could be determined from InSight data for events comparable to categories A through E, and sufficiently precise locations to reduce the distance effect in magnitude uncertainty to below 0.3 magnitude units for categories A, B, and E (Böse et al., 2018).

Moonquakes, deep and shallow

Seismic observation of Apollo has detected more than 13000 seismic events (Nakamura, 2003; see "Data and Resources"), encompassing endogenous moonquakes, meteorite impacts, and artificial sources.

The most frequent type of events is the deep moonquakes (DMQ) at depths between 700 *km* and 1100 *km* (Nakamura, 2005). They occur in clusters which are activated and deactivated in cycles corresponding to the orbital periods of the Moon-Earth-Sun system. Time lags between individual events of individual clusters are also not random (Bulow et al., 2007, Weber et al., 2010, and references therein). Kawamura et al. (2017) show that stress drops associated with DMQ are of the order of magnitude of the tidal stresses in their source regions. The DMQ are thus not only triggered but also caused by tidal stresses, i.e. the orbital motions in the Moon-Earth-Sun system can be considered as a part of the DMQ source mechanism. Since orbital motion is described by differential equations that allow evaluation forward and backward in time, the DMQ mechanism has a memory of the past and therefore cannot be i.i.d. Poissonian. The situation appears to be different for the (poorly understood) shallow moonquakes, which we discuss in section "Moon: High Frequency Teleseisms".

Therefore, we focus on shallow moonquakes in the following. The source mechanism of shallow moonquakes is not yet clear but they are likely to be caused by thermal contraction of the Moon (e.g. Binder & Lange, 1980), i.e. the same mechanism expected for marsquakes (Phillips, 1991, Knapmeyer et al., 2006, Plesa et al., 2018). If this is correct, shallow moonquakes can be regarded as lunar analogs of marsquakes.

Martian Seismotectonics

The seismic data available from Mars so far (up to late November 2018) contains only one candidate marsquake, which was recorded by the Viking 2 seismometer (Anderson et al., 1977), but could not iden-

tified as such unambiguously. At the time of writing, we are thus not in the possession of a seismic data set that allows for statistical evaluation. In this section we describe in more detail what is known about the seismotectonics of Mars, in order to support that out statistical approach is meaningful for Mars as well as for Earth.

After the successfuldeployment on December 19, 2018, broad band and short period seismic data from the InSight lander is expected to be received from January 2019 onwards. Routine evaluation of events, encompassing the identification of seismic phases, epicenter location based on multi-orbit surface waves and polarization analysis (Böse et al., 2017, Panning et al., 2015), will be conducted by a team at the Swiss Seismological Service located at ETH Zürich (Clinton et al., 2018), the Marsquake Service (MQS). Mars-specific magnitude scales were developed (Böse et al., 2018) and will be used by the MQS to quantify source strength on Mars. The event catalog produced by the MQS will also discriminate between different source types (tectonic, impacts, landslides, and atmospheric effects) based on the experience with Apollo data and physical differences in the source mechanism (see Daubar et al., 2018, concerning impacts, and Clinton et al., 2018, concerning the MQS).

Mars is a one-plate planet which shows no unambiguous indications of subduction zones or mid-ocean ridges, neither in topography nor in free air gravity anomalies or lithospheric magnetic field (e.g. Zuber et al., 2000, Hirt et al., 2012, Morschhauser et al., 2014). Nevertheless, it must have witnessed much seismic activity in the past, as its surface is crisscrossed with complex patterns of normal and thrust faulting. Knapmeyer et al. (2006) mapped more than 8500 normal and thrust faults with a cumulative length of about 680000 *km*, updated later on to approx. 14800 faults with a cumulative length of 940000 *km* (Knapmeyer et al., 2008). The shortest of these has a length of approx. 600 meters, while the longest graben that dissects the Tharsis bulge is almost 1450 *km* long. The Knapmeyer et al. (2006) fault catalog appears to be complete for faults longer than 80 *km*. The overall size-frequency distribution of Martian faults can be described by a power law with exponent well in the range found for fault popula-

tions on Earth (see Knapmeyer et al., 2006, and references therein). If one assumes that all fault segments are equally likely to break, and that large marsquakes require long breaking segments, then the length-frequency distribution of Martian faults is in favor for a power-law-like distribution of Marsquake sizes.

Taking the age of the youngest surface crossed by a fault as indicator of its age, no age preference for shorter or longer faults is found, i.e. the size frequency distribution appears to be independent of time. It must be noted, however, that 75 % or more of the total fault length was produced more than 3.5 Ga ago. The youngest faults are estimated to have an age of approx. 300 Ma.

Fault populations on Mars show features like fault linkage or relay ramps well known from Earth (see Schulz et al., 2010, and references therein, for a general treatment). The mechanisms of fault growth are considered to be the same on Earth and Mars (see Wyrick et al., 2018, for a recent analog study), although faults on Mars accumulate less displacement per length than faults on Earth. This can however be attributed to properties that all scale with gravity (Schulz et al., 2006).

Stresses resulting from differential cooling of the planetary interior are widely accepted as the main source of Martian seismicity (Phillips, 1991, Knapmeyer et al., 2006). Plesa et al. (2018) also investigated stresses resulting from mantle drag due to convection and found that these might under certain circumstances contribute significantly to the moment rate, and especially modify the regional distribution of effective stresses. Knapmeyer et al. (2006) defined end-member and "typical" models with "strong", "weak" and "medium" moment rates of $4.78 \times 10^{18}\ Nm/yr$, $3.42 \times 10^{16}\ Nm/yr$, and $5.99 \times 10^{16}\ Nm/yr$, respectively. Due to different corner moments, their models *StrongFew*, *StrongMany*, *WeakFew*, *WeakMany*, and *Medium* produce $m = 4$ events with recurrence rates between 13 hours and 6.7 years. Based on these and other estimations of martian seismcity, Panning et al. (2017) expect about 100 events per year that are detectable at distances beyond 60°.

While the Moon's seismic event rate is dominated by the deep moonquakes that are tied to Earth tides, Phillips (1991) found that although tidal loading by the sun produces high strain rates, the associated strains are small, and concluded that tidal loading of Mars is unimportant from the seismicity point of view. We expect that Mars, unlike the Moon, has no significant periodic seismicity.

Mars is well known for its giant volcanos. These have been active through much of the Martian history. Although some of the youngest volcanic surfaces might be only a few million years old(Neukum et al., 2004), no actual volcanic activity has ever been reported. The wristwatch pattern of faults around the Alba Patera volcano actually shows that its magma chamber retreated (Cailleau et al., 2003). Volcanic contributions to seismic activity are thus considered unlikely.

Fresh impacts have been found on Mars in images taken repeatedly from the same area (Malin et al., 2006), and might provide semi-controlled seismic sources when the location of an impact detected by a seismometer can be identified in imagery. Quantitative analysis shows that the recurrence intervals of globally detectable impacts is between one year and 10 years (Teanby & Wookey, 2011), where the longer intervals are expected to be more likely due to expected noise conditions. Contrary to an intuition one might have based on the cratered surface of especially the southern hemisphere of Mars, impacts are also not expected to dominate the seismic record.

Results

To assess the reliability of moment rate estimations we conduct numerical tests where we compare estimated rates with the GCMT catalog of earthquakes from the time interval 1976 to 2018 (section "Earth"), and also with the known true values of synthetic catalogs (section "Generic Synthetic Cata-

483 logs"). Finally, we generate synthetic catalogs for several models of Martian seismicity and investigate if
484 and how we can distinguish between them (section "Mars-specific synthetic catalogs").

485 Earth

486

487 Since the GCMT, as the most comprehensive and homogenous long-term catalog of moment tensor
488 solutions, relies on a global network of about 200 stations, we first need to establish that a single station
489 can provide data representative for Earth's global moment rate. The question here is what the global
490 completeness threshold for a single (broadband) seismometer is, and how long it takes until the largest
491 recorded event is above this completeness threshold.

492 We then compare how the output of different estimators evolves in time, i.e. re-evaluate all estima-
493 tors for each new event in the catalog throughout the time covered. Finally, we compare estimations for
494 different tectonic settings (subduction zones, mid-ocean ridges, and stable continental regions) by subdi-
495 viding the GCMT catalog according to Flinn-Engdahl-Zones and by evaluation of an additional catalog
496 dedicated to stable continental regions (as an analog for the single plate regime on Mars) which also
497 contains events predating the instrumental recording of earthquakes.

498 Since we will likely not be able to determine reliably the slope parameter of the martian seismicity
499 distribution, we use a fixed value of $\beta = 2/3$ throughout all these tests.

500 *Single Station Completeness Threshold*

501

502 We use as single station the temporary installation at Goldstone described in section "Temporary In-
503 stallation at Goldstone, CA". To find its completeness threshold, we compare the size-frequency (survi-
504 vor) distribution of events detected at Goldstone with the size-frequency distribution of the GCMT

(Figure 2). Distributions from short recordings are less smooth than that of the whole GCMT data base, and also differ between independent time windows of the same duration. In addition, the magnitude-to-moment conversion is based on empirical relations between uncertain quantities and may thus provide an uncertain moment value only, thus adding to the roughness of the curve. We therefore do not attempt to pin down the completeness threshold very precisely, but only estimate that it is somewhere between $10^{18}\ Nm$ and $10^{19}\ Nm$ for events of grade A alone, and possibly lower when taking A and B, or A, B, and E together. The GCMT lists 1273 events exceeding $10^{19}\ Nm$, and 5891 events exceeding $10^{18}\ Nm$, resulting in recurrence times of 12.2 and 2.7 days, respectively.

The strongest events in the grade A, $A \cup B$, and $A \cup B \cup E$ subsets are the same, so it is sufficient to use one of them fora moment rate estimation that relies on the strongest events. From the grade A events alone, we obtain a NLVR moment rate estimate of $1.03 \times 10^{22}\ Nm/yr$ ($m_S = 8.6$), while the KS_{10} estimator returns $5.79 \times 10^{21}\ Nm/yr$ ($m_S = 8.4$).

For comparison, we subdivide the GCMT catalog into 180 non-overlapping time windows, each of which has the same 86 days duration as the Goldstone experiment. Using the NLVR estimator we obtain a moment rate equivalent to magnitude 8.28 ± 0.42 from these time windows, while the KS_{10} estimator results in an equivalent magnitude of 8.25 ± 0.24.

Compared with the $7.61 \times 10^{21}\ Nm/yr$ ($m_S = 8.52$) obtained from the complete GCMT catalog, and comparing with Figure 3 and the KS_{10} emission probabilities in Figure 4, we conclude that the Goldstone experiment suffices to estimate the Earth's global seismic moment rate with acceptable accuracy.

One can thus expect that a seismometer installation comparable to the one at Goldstone produces a globally representative "largest event ever" time series three months or less after deployment, meaning that all comparable installations worldwide would produce the same such time series. For any longer recording time it is thus justified to evaluate the GCMT catalog instead of a single station catalog.

Moment Rate Estimations: Entire Earth

We compare the evolution in time of several different moment rate estimators. For this exercise we use only events from 1977 onwards since the GCMT completeness threshold for 1976 is significantly higher than for later years. We expect that the $NLVR$ and especially the KS_k estimators have a certain burn-in time: one cannot evaluate KS_k before having cataloged k events. Moreover, if the catalog contains events below the threshold for global detectability, the first listed events will not be representative for the global moment rate. By excluding 1976 from consideration we avoid mixing the burn-in time of the GCMT project with that of the rate estimation.

As a baseline we consider the summation of all events contained in the catalog between a time T_{start} and up to a time t, and divide by the number of years (assuming 365.25 days per year) elapsed between T_{start} and t to obtain an annual rate. The resulting time series $\dot{M}_{s,base}(t)$ is thus based on all data available at time t.

We compare this baseline with estimations based on the single strongest event ($\dot{M}_{s,NLVR}(t)$, based on the $NLVR$ estimator) and on the 2, 5, 10, and 50 strongest events ($\dot{M}_{s,KSk}(t)$, based on the KS_k estimator). The latter are computed only after a sufficient number of events is available, thus the respective time series start somewhat later than $\dot{M}_{s,base}(t)$ and $\dot{M}_{s,NLVR}(t)$. All time series are compiled in Figure 3.

A common feature of all time series is that they decay like $1/t$ or shallower as long as no large new contribution to the moment release occurs. This is of course most pronounced in $\dot{M}_{s,NLVR}(t)$, which can have a new peak only if an event occurs that is larger than any event before. But the effect is also clear in the $\dot{M}_{s,KSk}(t)$ time series, where smaller peaks indicate that new events entered the top-k list. Since new events can enter this list at any position, the value of the KS_k estimator will change more often with increasing k, hence the time resolution of $\dot{M}_{s,KSk}(t)$ increases with k.

In analogy to taking the absolute value of the difference between two values we compute

$$exp\left(\left|log\left(\dot{M}_{s,est}(t)\right) - log\left(\dot{M}_{s,base}(t)\right)\right|\right) \qquad (16)$$

to evaluate the deviation between an estimator and the baseline value, as it is sufficient to know that one of the two values has to multiplied by some factor to obtain the other one.

All estimators except KS_2, which sometimes overestimates by three orders of magnitude, follow the full-catalog baseline closely. Even the single-event $NLVR$ estimation never deviates by more than a factor of nine, as does KS_5. Both KS_{10} and KS_{50} are always within a factor 2.5 or less from the baseline, most of the time the factor is smaller than 2. When subdividing the GCMT into 21 consecutive, non-overlapping intervals of 2 years, the KS10 value is always within a factor 5 of the 42-years average, and within a factor 2 in half of all cases. All estimators tend to underestimate. We however do not think that the evaluation of a single catalog is sufficient to declare this a rule.

Moment Rate Estimations: Specific Tectonic Settings

Earth's seismicity is mainly due to plate tectonics, and by far most of its seismicity (approximately 75 % of all events) occurs at active plate boundaries. Subduction zones alone account for approximately 60 % of all earthquakes. Mars, on the other hand, is a one-plate planet. It is thus desirable to investigate if reasonable moment rate estimations can be made for selected, either Earth specific or Mars specific tectonic settings rather than for the entire Earth.

Based on the Flinn-Engdahl regionalization scheme of seismic regions (Young et al., 1995), we extract events belonging to mid-ocean ridges and subduction zones from the GCMT according to the region IDs listed in the appendix 0. Since the F-E-Regions define regions on the Earth's surface but not in its interior, we further subdivide the events classified as "subduction zone" into two depth layers, above and below 100 km, in order to clearly separate subducting slabs from crustal events. The number of events sorted into each of the four resulting groups of events is given in Table 3.

As reported earlier (e.g. Bird & Kagan, 2004), the distribution for mid-ocean ridge events appears to be significantly steeper than for the other groups (Figure 5**Fehler! Verweisquelle konnte nicht gefunden werden.**), the slopes of which appear to be essentially identical with that obtained for the complete catalog. Especially a test using mid-ocean ridge events is thus a scenario different from the other groups, or the GCMT taken as a whole.

For each group we evaluate (a) the sum of all events divided by the number of years covered by the catalog (42.3 years), (b) the $NLVR$ estimator, and (c) the KS_{10} estimator, thus obtaining three values for each group. The resulting moment rates, expressed both in Nm/yr and as moment magnitude of a single event releasing the same amount of seismic moment, are also summarized in Table 3.

In most cases, both the $NLVR$ and the KS_{10} estimator underestimate the value obtained by summing up all events of a subset. The ratios between these estimators and the complete summation are well in the range found for the entire Earth. This holds for all four subsets.

Thus the results obtained for the GCMT are encouraging, but we note that an evaluation of a station installed e.g. in early 2004 would look different, since its event catalog would report two very strong events (Banda Aceh and Tohoku) within only 6 years.

Neither subduction zones nor mid ocean ridges exist on Mars. We thus use the Earthquake Catalog for Stable Continental Regions of Schulte & Mooney (2005, see also "Data and Resources") as a better analog of martian seismicity.

We subdivide the catalog into two groups: the first contains events for which no instrumental record is available, while the second contains events that were interpreted solely based on instrumental records (a third group of events, where historical information and instrumental data is interpreted together, was excluded from our analysis). The goal is to compare moment rate estimations resulting from the historical events with independent estimations for the instrumental epoch.

We do not consider the 21 events listed for the time between 495 AD and 1500 AD (only three of which occurred before 1000 AD). This may look like a somewhat arbitrary modification of the catalog, but we think it is justified since an extension of the covered period by 1000 years biases the duration of observation in a more severe way than the omission of 21 events with moment magnitudes below 6.1 biases the released seismic moment. We also delete two reservoir-associated events that occurred in India in 2000, since the catalog assigns unlikely seismic moments beyond $10^{23}\ Nm$ (corresponding to $M_W > 9$) to both of them, which are also in clear contradiction with the listed magnitude values (around 5). We thus obtain 226 events from 1500 AD to 1949 and 879 events from 1950 to 2003. Their size-frequency distributions are shown in Figure 5. Here the group of historical events shows a much lower slope than all other distributions shown. This is a property expected for incomplete catalogs, as this historical events list certainly is. The slope of the distribution of the instrumentally evaluated events is very similar to that of the GCMT, but this is not surprising since many of the corresponding catalog entries are based on the GCMT.

The resulting moment rate estimates are consistent within each of the two groups (see Table 3), but the values obtained for the events from the instrumental epoch are also consistently higher than those for the historical events, by factors between 1.7 and 4.1, with the $NLVR$ estimator producing the largest deviation. Although these deviations are still in the range of variability seen for the different estimators in Figure 3, they exhibit a certain trend. If expressed as magnitudes, we find that the differences between the individual estimates is no larger than the uncertainty attributed to the individual magnitude estimations as listed in the catalog, which is typically 1 magnitude unit, and never below 0.4 magnitude units.

In summary we find that the evaluation of the GCMT is encouraging, although it was purely accidental that its largest events occurred late. The deviations obtained with the Stable Continental Regions catalog might be attributed to the very circumstantial nature and general uncertainty of historic observations,

but might also point to a systematic shortcoming of our approach. To further investigate bias and variance of our estimators, we conduct an extensive series of tests with synthetic catalogs.

Moon: High Frequency Teleseisms

For the shallow moonquakes, we use here the seismic moments estimated by Oberst (1987). In total, 28 shallow moonquakes were detected by the Apollo network. We evaluated the annual seismic moment release of the following subsets: 1) All shallow moonquake events; 2) Events during 1972-1973; 3) Events during 1974-1975; 4) Events during 1976-1977; 5) Events during 1973-1974; 6) Events during 1975-1976. We tested if the seismic moment release evaluated from two-years subsets differ or agrees with that obtained from the complete observation period. We also tested how fast the obtained seismic moment converges to the reference value obtained with the full dataset. We reevaluate the seismic moment release every time a new shallow moonquake is detected and studied the evolution of obtained seismic moment rates like with the GCMT. The results are summarized in Figure 6. KS_{10} Emission probabilities for the moment rate resulting from all shallow moonquakes together are shown in Figure 7. The maximum emission probability coincides with the rate obtained from all events. In the case of the Moon, the scattering of obtained seismic moment rate is rather small and the difference is about 50% in maximum. The small deviation is likely to be due to the smaller range of magnitude (from $4.7 \times 10^{12}\ Nm$ to $1.6 \times 10^{15}\ Nm$) and the small number of events for shallow moonquakes. Likewise, the seismic moment rate converged relatively quickly after 4-5 events. Unlike on the Earth, the possible source of excitation is limited and result in smaller variety of events. This may be the case on Mars as well, allowing to obtain a representative seismic moment rate rapidly.

Generic Synthetic Catalogs

We set up a logarithmically equidistant grid of M_S and M_c values via an equidistant grid of equivalent magnitudes. We vary m_S from 3 to 10 in steps of 0.1 magnitude units. The equivalent magnitude of the

corner moment is varied relative to m_S from $m_S - 4$ to $m_s + 4$, also in steps of 0.1 magnitude units. This results in a $81 \times 71 = 5751$ elements matrix of combinations of moment rates and corner moments.

The resulting event rates, computed for an assumed completeness threshold magnitude $m_t = 2$ range from 10^{-216} to 10^9 events per year (some parameter combinations result in even smaller rates that were not numerically resolvable, these cases were excluded from the simulation process). Neither of these extremal values is suitable to produce meaningful catalogs. We therefore adjust the completeness threshold individually for each combination of moment rate and corner moment in order to obtain catalogs of uniform sizes for all cases. A simple iterative search scheme is used to solve eq. 3 for M_t numerically for this purpose. In analogy to the planned life time of the InSight mission, we generate catalogs covering 2 terrestrial years (or 730 terrestrial days), each containing approximately 10000 events (in a few cases, where this requires $m_t > m_c$, we force $m_t < m_c$ and obtain catalogs with about 10^5 events).

The result of any moment rate estimation will depend on the individual realization of the catalog generator, depending on what the largest cataloged event actually is. To analyze the resulting variability of the estimated moment rate, we thus generate a total of 1410 catalogs (a number chosen with respect to the overall computation time) for each of the 5751 parameter combinations, resulting in approximately eight million usable catalogs. The complete simulation can be run overnight on a desktop PC.

For each catalog, we evaluate the NLVR and KS_{10} estimators and record the resulting bias between the moment rate's equivalent magnitude m_s used during catalog generation and the estimated value's equivalent magnitude m_{est}, defined as

$$\mathrm{m}_{bias} = \mathrm{m}_S - \mathrm{m}_{est} \qquad (17)$$

i.e. the bias is positive for underestimation. From the biases obtained for catalogs resulting from the same value of the ratio M_S/M_c (or from the same difference $m_S - m_c$) we construct distribution densities, median values and the boundaries of 95% quantiles centered around the median, i.e. intervals which contain 95% of all bias values.

Estimation with correct slope

In a first test, we use the same slope $\beta \in \{0.4, 0.5, 0.6, 0.625, 2/3\}$ during catalog generation as well as during the evaluation. We generate independent sets of approximately 8 million catalogs for the evaluation using either the NVLR estimator or the KS_{10} estimator. Since we already established that the KS_k estimator gets better with increasing k, we now use a fixed value of $k = 10$ which is realistic for Mars and expected to perform well in the light of the evaluation of the GCMT.

If the corner moment is known (which can be expected only in synthetic cases) a two-dimensional histogram relating the bias between true and estimated moment rate to the difference $m_S - m_C$ can be constructed (left panels in Figure 8 (NLVR) and Figure 9 (KS_{10})). Individual moment rate estimates may vary strongly between individual catalogs, by as much as three or more units of equivalent magnitude. The ratio M_S/M_c controls systematic variations of distribution median and width, and NLVR and KS_{10} show different behavior: While the NLVR estimator shows the greater variance for $m_S - m_C < 0$, the variance of the KS_{10} estimator is larger for $m_S - m_C > 0$. Both estimators are near unbiased if $m_S = m_C$.

If the correct value of $m_S - m_c$ is unknown, the 2D distribution densities depicted in the left panels of Figure 8 and Figure 9 reduces to the marginal densities depicted in the right panels. These show that, for $\beta = 2/3$, the probability of overestimating the moment rate is approximately 10% for the NLVR estimator, and 41% for the KS_{10} estimator. The probability that the estimated value is within ± 1 magnitude

686 units of the true value is 49 % for the NLVR estimator, and 72% for the KS_{10} estimator for the given
687 range of possible $m_S - m_c$ differences.

688 These percentages depend on the value of the slope parameter β and increase as β increases. As Fig-
689 ure 10 (NLVR) and Figure 11 (KS_{10}) show, the distribution densities get narrower and more symmetric
690 with increasing β: The probability that the estimated moment rate is within ± 1 magnitude units from
691 the true value increases as the distribution narrows, and the probability of an overestimation increases
692 as the distribution become more symmetric about the zero bias.

693 ***Estimation with incorrect slope***

694 As mentioned in the introduction, estimating the slope parameter from a single station catalog is like-
695 ly biased towards small slopes, since only a fraction of the smaller events will be observed. Since both of
696 our moment rate estimators make use of the slope, we must ask how sensitive the outcome is to an in-
697 correctly guessed slope.

698 We again generate catalogs with a true slope of $\beta \in \{0.4, 0.5, 0.6, 0.625, 2/3\}$, but use the same set
699 of values used for the estimation from our synthetic catalogs. We thus obtain a matrix of true and as-
700 sumed slopes and evaluate the fraction of moment rate estimates that falls within ± 1 or ± 2 magnitudes
701 from the true value, and also how likely we overestimate the actual moment rate. As before, we evalu-
702 ate approximately 8 million catalogs for each combination of true and assumed slope parameter.

703 In Figure 12 we show the resulting percentages, i.e. the width of distribution densities as shown in
704 Figure 10 and Figure 11, for both the NLVR (top) and KS_{10} (bottom) estimator. Although the width pa-
705 rameters depend on both the true slope and the slope assumed by the estimator, the influence of the
706 latter on the number of cases where the estimated moment rate is within ± 1 or ± 2 magnitudes from
707 the true value is much smaller than that of the true slope. It is thus sufficient if the assumed slope is ap-
708 proximately correct within a relatively wide range. This holds for both estimators.

A notable difference is the fraction of cases where the actual moment rate is overestimated: For the NLV estimator, this fraction depends mainly on the assumed slope and not as much on the true slope, whereas it is about equally sensitive on both values for the KS_{10} estimator.

Mars-specific synthetic catalogs

The tests described so far indicate that variance and bias of both the NLVR and the KS_k estimator are such that we cannot expect to solve the question of the Martian moment rate unambiguously, by inverting some estimated value into a best fitting rate. The emission probability approach using a search grid of moment rates and corner moments is more promising.Here we investigate in how far it is possible to distinguish hypothetical states by these emitted rate estimates, and in how far longer experiment life times support this distinction.

We consider the five end-member seismicity models of Knapmeyer et al., (2006), which mark some extreme corners of their parameter space. These models were named *WeakFew*, *WeakMany*, *Medium*, *StrongFew*, and *StrongMany* according to their relative moment rates (weak, medium or strong) and event rates (few, medium, or many). Since Knapmeyer et al. (2006) use the truncated rather than the tapered Gutenberg-Richter distribution, we have to convert their maximum seismic moment M_{Max} into corner moments M_C in order to keep the moment rate unchanged when switching to the tapered distribution, using

$$M_C = M_{Max}\left[\frac{\beta}{\Gamma(2-\beta)}\right]^{1/(1-\beta)} \qquad (18)$$

after Kagan (2002b). The conversion factor amounts to approximately 0.416 for $\beta = 2/3$, or 0.391 for $\beta = 0.625$ as used in the five models. Moment rates and corner moments of the models are summarized in Table 4. It is worth noting that $m_S - m_C$, which proved crucial for variance and bias of the estimators

in the previous tests, is negative for the *StrongFew*, *Medium*, and *WeakFew* models (but close to zero for Medium), but positive for the *StrongMany* and *WeakMany* models (rightmost column of Table 4).

To assess the effect of experiment life time, we consider catalogs covering 1, 2, 4, 8, 16, and 32 (earth) years. The exponential increase of durations was chosen in order to compensate for the power law decay of event probabilities with magnitude. Considering even longer times appears to be unnecessary, since no lander with such a life time is known, and since we hope that improved follow-up experiments will make the entire discussion obsolete at some time.

We generate 10^6 catalogs, with approximately 10000 events per catalog, for each duration, and thus obtain six different probability density functions for estimated moment rates for each of the five models. We repeat this for both the NLVR and the KS_{10} estimator and compare the resulting probabilities graphically (Figure 13 and Figure 14). Independent realizations are used for the two estimators, but given the smooth PDFs that we obtain, we are convinced that this does not affect our results.

For both estimators, doubling the experiment life time moves the maximum of the histograms (i.e. the mode) in Figure 13 and Figure 14 by a constant amount towards larger values (meaning a multiplication by a constant factor on the seismic moment scale). This shows that the choice of an exponential series of life times was appropriate to investigate the long term behavior.

The NLVR and KS_{10} estimators however show a significant difference concerning the width (i.e. standard deviation) of the distributions: While the NLVR distributions become narrower in most cases (not very much in the case of the *WeakFew* model, left hand side of Figure 15), the KS_{10} standard deviation decreases not as much, or even grows (in the case of the *WeakMany* and *StrongMany* models, right hand side of Figure 15).

The changes in mode and standard deviation of NLVR work together in such a way that probabilities left of the maximum decrease quickly with time, while probabilities right of the maximum increase only

slowly with time. This makes the evolution of the curves look like a caterpillar pulling its rear end towards the head before moving its head forward.

The KS_{10} estimator behaves differently: here the whole curve moves towards the right essentially unchanged like the shell on the back of a crawling snail, with the notable exception of the *StrongMany* model which behaves like a caterpillar pushing its head forward towards the right with its tail fixed (Figure 14).

The two estimators also behave differently when it comes to the rejection of models.

After two years of registration, NLVR moment rate estimates between $2 \times 10^{16}\ Nm$ and $1.3 \times 10^{18}\ Nm$ (equivalent magnitudes $m_S$between 4.8 and 6) would be rather inconclusive, since all five models have significant probabilities to produce estimates in this range. An estimated rate of less than $3.9 \times 10^{16}\ Nm$ ($m_S = 5$) would exclude the *StrongMany* model. A NLVR estimation below $1 \times 10^{16}\ Nm$ ($m_S = 4.6$) would additionally exclude the *Medium* and *StrongFew* models. A NLVR result larger than $1.6 \times 10^{17}\ Nm$ ($m_S = 5.4$) obtained after two years, on the other hand, would exclude the *WeakFew*, *WeakMany* and *StrongMany* models.

With the KS_{10} estimator, the *StrongMany* model could be excluded if the rate estimate is below $8.9 \times 10^{17}\ Nm$ ($m_S = 5.9$). KS_{10} estimates below $5.6 \times 10^{16}\ Nm$ or above $1.6 \times 10^{17}\ Nm$ (m_S between 5.1 and 5.4) are crucial to distinguish between the *WeakMany*, *Medium*, and *StrongFew* models. More such thresholds could be identified.

As a sketch for the application to InSight data, we simulate a single two years catalog for the Knapmeyer et al. (2006) *Medium* scenario with parameters as given in Table 4, and evaluate the KS_{10} estimator. This results in an estimated moment rate of $2.72 \times 10^{17}\ Nm/yr$. The emission probability map favors moment rates close to the one used for catalog generation, and clearly allows the rejection of a moment rate as low as the Moon's (Figure 16). Based on the simulated catalog, a moment rate as high as

776 the Earth's could only be accepted when assuming that marsquakes larger than the largest known earth-
777 quakes are possible.

778 The following observations are crucial here: Firstly, in principle, it is possible to reject at least some of
779 the Knapmeyer et al. (2006) models using the NLVR estimator alone. Second, the moment rate thresh-
780 olds to exclude models evolve with time, i.e. with the time span covered by the catalog. And third,
781 thresholds excluding individual models differ between the NLVR and KS_{10} estimators. Also, the use of the
782 KS_{10} estimator was a decision made here to keep the amount of tests to run in a reasonable range. If
783 more events become available, there is however no reason not to use them for a $KS_{k>10}$ estimation. It is
784 thus meaningful to use different estimators in parallel, and to also track the evolution of the estimators
785 with time.

786 # Discussion

787 Our tests with terrestrial data demonstrate that the Earth's moment rate can be estimated from a
788 single, short-lived broadband station, even if it is a temporary installation rather than being placed in a
789 state of the art observatory shelter (the Lorenz et al., (2015) installation at Goldstone serves as an exam-
790 ple). The list of the largest *k* events becomes representative within a few weeks. This minimum time
791 frame of course depends on the actual moment and event rates and is likely longer on Mars. It will be a
792 crucial exercise to determine from the observations what the duration of this "burn in" time on Mars is.
793 Besides the usual methods to determine the completeness threshold of catalogs, a comparison of the
794 actual Mars catalog with modeled detection probabilities might be useful. For the Earth, the moment
795 rate can be estimated to within a factor 2.5 or better after a burn in of less than 2 weeks from the 10
796 largest events (Figure 3).

A subdivision of Earth's seismicity into specific tectonic settings (subduction zones, subducting slabs alone, mid-ocean ridges, stable continental regions) still allows estimating the moment rate of these regions within the uncertainty of the seismic moments of the individual events used. For the stable continental settings we however obtain larger deviations, indicating that either the approach is less reliable than the whole-GCMT results suggest, or that the estimators show a significant variance.

To assess more generic properties of our estimators, we conduct a series of Monte Carlo experiments, simulating seismicity catalogs for a variety of parameters, and compare the estimated moment rates with the known values used for the simulation.

The estimation of the uncertainty of the bias estimate critically depends on the assumed range of M_S/M_C, while knowledge of the slope β is of minor importance, thus allowing to use a generic value like $\beta = 2/3$. To our best knowledge, there is no self-consistent limitation of M_S/M_C in the origins of the tapered Gutenberg-Richter distribution. Maximum likelihood estimation of M_C often produces a lower limit only (Bird & Kagan, 2004), and any estimator will suffer from the fact that the necessary large events are also the most rare ones. Thus giving a range of M_S/M_C is hardly possible in advance and will remain challenging in the course of the experiment, as far as the InSight mission to Mars is concerned. We limited the difference of equivalent magnitudes to $|m_S - m_C| < 4$, motivated by the range $-2.4 < m_S - m_C < 1.7$ found with the end-member models of Knapmeyer et al. (2006), and adding some margin.

A physical argument creating an upper limit for the corner moment arises from geological considerations on the largest possible event, as discussed in section "Seismic Moment Rate Estimation" for the Earth, assuming an event with a fault plane as large as the planet's surface.

The estimation for the seismic moment upper bound used there scales with R^3, thus the corresponding estimation for Mars is about 15% of that obtained for Earth, or $10^{28} Nm$ (or $M_W = 12.6$). The crater-

ing record and derived surface ages for Mars show that no event involving the entire Martian surface occurred during the recent 3.8 billion years or so (taking the systematic age difference between Hesperian northern lowlands and Noachian southern highlands as a reference for the creation of the dichotomy, whatever caused it), the longest faults of Knapmeyer et al., (2006) actually suffice for $M_W \approx 9$ if the entire fault breaks in a single event. We thus predict that the corner moment of the Martian quake statistic is such that events of $M_W = 12.6$ do practically not occur in the sense of the discussion in section "Seismic Moment Rate Estimation", i.e. that the corner moment is at least one magnitude below $10^{28} Nm$ and does not exceed $10^{25} Nm$ (this is however a weak prediction given that the Knapmeyer et al. (2006) models hardly exceed $10^{20}\ Nm$ for good reasons).

The InSight mission will have to deal with a physically reasonable subset of all possible parameters. Testable predictions that can be challenged individually by InSight data have been made in the literature, and a determination of the moment rate sufficiently accurate to reject some models would be a significant achievement.

Our simulations reveal that both the NLVR and KS_k estimations show considerable biases and variances. Nevertheless the NLVR estimator, as the most simple one, will allow constraining the actual moment rate of Mars when comparing its output with simulated distributions of given seismicity models. Depending on experiment life time and the chosen estimators, threshold exists that clearly discriminate between the Knapmeyer et al. (2006) models. The most promising approach for the interpretation of moment rate estimates appears to be to scan the moment-rate-corner-moment state space like in Figure 4, Figure 7, and Figure 16, and determine the probability that a certain state emits the moment rate estimated from observed events.

Our approach relies on several assumptions:

- Marsquakes are i.i.d. events resulting from a Poisson process.

- Their size-frequency distribution can be described by the Tapered Gutenberg-Richter distribution.
- The slope of the distribution is such that the moment rate is governed by the strongest, rather than by the smallest, events i.e. $\beta < 1$.
- A reasonable guess for the slope is $\beta = 2/3$.
- Martian moment rate and corner moment are sufficiently high to allow for the detection of at least a few globally representative events, or, in other words, InSight's detection threshold will be low enough that some threshold magnitude exists above which the Marsquake catalog will be complete.

It might not be possible to test all these assumptions with InSight data alone. Establishing the validity of the Tapered Gutenberg-Richter distribution, for example, will likely require much longer observation times and more than one station – even the decade-long catalogs available for Earth do not yet provide a clear picture of the distribution of the strongest earthquakes. All these assumptions, however, can be tested in principle. We intend to evaluate several additional diagnostics based on event location and distribution of events in time to assess the validity of our assumptions.

Conclusion

Statistics is best when it is based on a large data set. The boundary conditions of interplanetary missions however make it challenging to obtain quake catalogs comparable to the GCMT. We nevertheless have to make the most of whatever data we obtain.

With equations (2) and (3), the tapered Gutenberg-Richter distribution of quakes is described by slope β, corner moment M_C, moment rate $\dot{M}_S$, and an observer-dependent completeness threshold moment M_t. While we frequently find statements in the literature that thousands of quakes are neces-

sary to determine slope and corner moment reliably, we have discussed ways to estimate the moment rate based on sparse observations.

Two distinct approaches are proposed, the NLVR estimator which relies on the single largest event ever observed, and the KS_k estimator, which evaluates the $k > 1$ largest events.

We have evaluated the performance of both estimators numerically. First we apply them to the current GCMT catalog, covering the time from January 1976 to May 2018 and containing nearly 50000 earthquakes. Secondly, we use synthetic catalogs generated from the Tapered Gutenberg-Richter distribution and represented by a total of more than 560 million catalogs worth of almost 2.5 billion years of simulated seismicity.

We find that the proposed estimators will allow rejecting at least some of the published seismicity models by their predicted moment rates. The uncertainty of the estimates depends on $\dot{M}_S/M_C$, but is sufficiently small to discriminate several published seismicity models even after only two years mission life time on Mars.

Data and Resources

The Apollo seismic event catalog can be found at http://www-udc.ig.utexas.edu/external/yosio/PSE/catsrepts/

The Global Centroid Moment Tensor was retrieved from IRIS, https://ds.iris.edu/ds/products/momenttensor/ on 17. May 2018.

Waveform data from the Goldstone experiment was obtained from Lorenz et al. (2015), we kindly refer to their Data and Resources section.

The Stable Continental Regions catalog of Schulte & Mooney (2005) was retrieved from the USGS at https://earthquake.usgs.gov/data/scr_catalog.php, last accessed 12. June 2018.

The coordinates of Flinn-Engdahl region boundaries was retrieved from USGS, at ftp://hazards.cr.usgs.gov/web/hazdev-geoserve-ws/FE/, last accessed 15.05.2018

Acknowledgements

We wish to thank Associate Editor Nicholas van der Elst, Peter Bird (UCLA) and two anonymous reviewers for their comments which helped to clarify the manuscript. We are also grateful to Betty Schiefelbein of the BSSA editorial office for generous support concerning formatting issues.

This work benefitted from discussions within the InSight SEIS science team, and especially R. Widmer-Schnidrig of Black Forest Observatory and D. Giardini of ETH Zürich.

A portion of the work was supported by the InSight Project at the Jet Propulsion Laboratory, California Institute of Technology, under a contract with the National Aeronautics and Space Administration.

R.C.Weber was supported by the NASA InSight project, contract NNH10ZDA007O.

N. Teanby was supported by the UK Space Agency.

This is InSight Contribution Number 77.

References

Anderson, D.L., Miller, W.F., Latham, G.V., Nakamura, Y., Toksöz, M.N., Dainty, A.M., Duennebier, F.K., Lazarewicz, A.R., Kovach, R.L., Knight, T.C.D. (1977). Seismology on Mars, J. Geophys. Res., vol. 82, No. 28, 4524-4546

Banerdt, W.B., Smrekar, S., Hurst, K., Lognonné, P., Spohn, T., Asmar, S., Banfield, D., Boschi, L., Christensen, U., Dehant, V., Folkner, W., Giardini, D., Goetz, W., Golombek, M., Grott, M., Hudson, T., Johnson, C., Kargl, G., Kobayashi, N., Maki, J., Mimoun, D., Mocquet, A., Morgan, P., Panning, M., Pike, W.T.,

907 Tromp, J., van Zoest, T., Weber, R., Wieczorek, M. and the InSight Team, (2013). InSight: A discovery mis-
908 sion to explore the interior of Mars, 44th., Lunar Planet. Sci. Conf., abstract 1915

909 Binder, A.B., Lange, M.A. (1980). On the thermal history, thermal state, and related tectonism of a Moon
910 of fission origin; J. Geophys. Res., vol. 85, B6, 3194-3208

911 Bird, P.; Kagan, Y.Y. (2004) Plate-Tectonic analysis of shallow seismicity: apparent boundary width, beta,
912 corner magnitude, coupled lithosphere thickness, and coupling in seven tectonic settings, Bull. Seis. Soc.
913 Am., vol. 94, No. 6, 2380-2399

914 Bormann, P., Baumbach, M., Bock, G., Grosser, H., Choy, G.L., Boatwright, J. (2002). Chapter 3: Seismic
915 Sources and Source Parameters, In: Bormann, P. (Ed.)(2002) IASPEI New Manual of Seismological Obser-
916 vatory Practice, GeoForschungszentrum Potsdam, vol. 1

917 Böse, M., Clinton, J., Ceylan, S., Euchner, F., van Driel, M., Khan, A., Giardini, D., Lognonné, P., Banerdt,
918 W.B., (2017) A probabilistic framework for single-station location of seismicity on Earth and Mars, Phys.
919 Earth Planet. Inter., vol. 262, 48-65, doi:10.1016/j.pepi.2016.11.003

920 Böse, M., Giardini, D., Stähler, S., Ceylan, S., Clinton, J.F., van Driel, M., Khan, A., Euchner, F., Lognonné,
921 P., Banerdt, W.B. (2018), Magntiude scales for Marsquakes, Bull. Seis. Soc. Am., vol. 108, No. 5A, 2764-
922 2777, doi: 10.1785/0120180037,

923 Bulow, R.C., Johnson, C.L., Bills, B.G., Shearer, P.M. (2007) Temporal and spatial properties of some deep
924 moonquake clusters, J. Geophys. Res., vol. 112, doi:10.1029/2006JE002847

925 Cailleau, B., Walter, T.R., Janle, P., Hauber, E. (2003) Modeling volcaninc deformation in a regional stress
926 field: Implications for the formation of graben structures on Alba Patera, Mars, J. Geophys. Res., vol. 108
927 (E12), 5141, doi:10.1029/2003JE002135

928 Clinton, J., Giardini, D., Böse, M., Ceylan, S., van Driel, M., Euchner, F., Garcia R.F. Kedar, S., Khan, A.,
929 Stähler, S.C., Banerdt, B., Lognonné, P., Beucler, E., Daubar, I., Drilleau, M., Golombek, M., Kawamura, T.,
930 Knapmeyer, M., Knapmeyer-Endrun, B., Minoun, D., Mocquet, A., Panning, M., Perrin, C., Teanby, N.A.
931 (2018) The Marsquake Sercive: Securing Daily Analysis of SEIS Data and Building the Martian Seismicity
932 Catalogue for InSight, Space Sci. Rev., vol. 214, doi:10.1007/s11214-018-0567-5

933 Cooper, M.R., Kovach, R.L. (1975). Energy, frequency, and distance of moonquakes at the Apollo 17 site,
934 Proc. Lunar Sci. Conf. 6th, pp. 2863-2879

935 Daubar, I., Lognonné, P., Teanby, N.A., Miljkovic, K., Stevanivić, J., Vaubailln, J., Kenda, B., Kawamura, T.,
936 Clinton, J., Lucas, A., Drilleau, M., Yana, C., Collins, G.S., Banfield, D., Golombek, M., Kedar, S., Schmerr,
937 N., Garcia, R., Rodriguez, S., Gudkova, T., May, S., Banks, M., Maki, J., Sansom, E., Karakostas, F., Panning,
938 M., Fuji, N., Wookey, J., van Driel, M., Lemmon, M., Ansan, V., Böse, M., Stähler, S., Kanamori, H.,
939 Richradson, J., Smrekar, S., Banerdt, W.B., (2018), Impact-Seismic Investigations of the InSight Mission,
940 Space Sci. Rev., vol. 214, doi: 10.1007/s11214-018-0562-x

941 Dziewonski, A. M., Chou, T.-A., Woodhouse, J.H (1981), Determination of earthquake source parameters
942 from waveform data for studies of global and regional seismicity, J. Geophys. Res., vol. 86, 2825-2852,
943 doi:10.1029/JB086iB04p02825

944 Ekström, G., Nettles, M., Dziewonski, A.M. (2012), The global CMT project 2004-2010: Centroid-moment
945 tensors for 13,017 earthquakes, Phys. Earth Planet. Inter., vol. 200-201, 1-9,
946 doi:10.1016/j.pepi.2012.04.002

947 Gardner, J.K.; Knopoff, L. (1974). Is the Sequence of Earthquakes in Southern California, with Aftershocks
948 removed, Poissonian?, Bull. Seism. Soc. Am., vol. 64, No. 5, 1363-1367

949 Godano, C., Pingue, F. (2000). Is the seismic moment-frequency relation universal?, Geophys. J. Int., vol.
950 142, 193-198

951 Golombek, M.P., Banerdt, W.B., Tanaka, K.L, Tralli, D.M. (1992). A prediction of mars seismicity from
952 surface faulting, Science, vol. 258, No. 5084, 979-981

953 Golombek, M.P. (2002). A revision of Mars seismicity from surface faulting, Lunar Planet. Sci. Conf.,
954 XXXIII, Abstract 1244

955 Golombek, M., Kipp, D., Warner, N., Daubar, I.J., Fergason, R., Kirk, R.L., Beyer , R., Huertas, A., Piqueux,
956 S., Putzig, N.E., Campbell, B.A., Morgan, G.A., Charalambous, C., Pike, W.T., Gwinner, K., Calef, F., Kass,
957 D., Mischna, M., Ashley, J., Bloom, C., Wigton, N., Hare, T., Schwartz, C., Gengl, H., Redmond, L., Tra-
958 utmann, M., Sweeney, J., Grima, C., Smith, I.B., Sklyanskiy, E., Lisano, M., Benardini, J., Smrekar, S.,
959 Lognonné, P., Banerdt, W.B. (2017) Selection of the InSight Landing Site, Space Sci. Rev., vol. 211, 5-95,
960 DOI 10.1007/s11214-016-0321-9

961 Gutenberg, B., Richter, C.F. (1941). Seismicity of the Earth, in: Seismicity of the Earth, Geological Society
962 of America Special papers No. 34, Geological Society of America, New York, 1-126

963 Gutenberg, B., Richter, C.F. (1944). Frequency of earthquakes in California, Bull. Seis. Soc. Am., vol. 34,
964 No. 4, 185-188

965 Hathi, B., Ball, A.J., Colombatti, G., Ferri, F., Leese, M.R., Towner, M.C., Withers, P., Fulchigioni, M., Zar-
966 necki, J.C. (2009). Huygens HASI servo accelerometer: A review and lessons learned, Planetary and Space
967 Science, vol. 57, 1321-1333, doi:10.1016/j.pss.2009.06.023

968 Hirt, C., Claessens, S.J., Kuhn, M., Featherstone, W.E. (2012) Kilometer-resolution gravity field of Mars:
969 MGM2011, Planet. Sp. Sci., vol. 67, 147-154, doi:10.1016/j.pss.2012.02.006

970 Kagan, Y.Y, (1997). Seismic moment-frequency relation for shallow earthquakes: regional comparison, J.
971 Geophys. Res., vol. 102, B2, 2835-2852

972 Kagan, Y.Y. (1999). Universality of the Seismic Moment-frequency Relation, Pure Appl. Geophys., vol.
973 155, 537-573

974 Kagan, Y.Y. (2002a). Seismic Moment Distribution revisited: I. Statistical results. Geophys. J. Int., vol. 148,
975 520-541

976 Kagan, Y.Y. (2002b). Seismic moment distribution revisited: II. Moment conservation principle, Geophys.
977 J. Int. vol. 149, 731-754

978 Kagan, Y.Y. (2014). Earthquakes. Models, Statistics, Testable Forecasts, American Geophysical Union,
979 Wiley, 283 pages

980 Kagan, Y.Y., Schoenberg, F. (2001). Estimation of the upper cutoff parameter for the tapered pareto dis-
981 tribution, J. Appl. Probab., vol. 38A, 158-175

982 Kawamura, T., Lognonné, P., Nishikawa, Y., Tanaka, S. (2017), Evaluation of deep moonquake source
983 parameters: Implication for fault characteristics and thermal state, J. Geophys. Res. Planets, vol. 122,
984 1487-1504, doi:10.1002/2016JE005147

985 Knapmeyer, M., Schneider, S., Misun, M., Wählisch, M., Hauber, E. (2008) An extended global inventory
986 of Mars Surface Faults, Geophysical Research Abstracts, vol. 10, EGU2008-A-03574

987 Knapmeyer, M., Fischer, H.-H., Knollenberg, J., Seidensticker, K.J., Thiel, K., Arnold, W., Schmidt, W.,
988 Faber, C., Finke, F., Möhlmann, D. (2016). The SESAME/CASSE instrument listening to the MUPUS PEN

989 insertion phase on comet 67P/Churyumov–Gerasimenko, Acta Atronautica, vol. 125, 234-249, doi:
990 10.1016/j.actaastro.2016.02.018

991 Knapmeyer, M., Oberst, J., Hauber, E., Wählisch, M., Deuchler, C., Wagner, R. (2006). Working models for
992 spatial distribution and level of Mars' seismicity, J. Geophys. Res., vol. 111, E11006,
993 doi:10.1029/2006JE002708

994 Knapmeyer-Endrun, B., Golombek, M. P., and Ohrnberger, M., 2017, Rayleigh wave ellipticity modeling
995 and inversion for shallow structure at the proposed InSight landing site in Elysium Planitia, Mars: Space
996 Science Reviews, v. 211, p. 339-382, DOI: 10.1007/s11214-016-0300-1

997 Ksanfomaliti, L.V., Zubkova, V.M., Morozov, N.A., Petrova, E.V. (1982), Microseisms at the Venera 13 and
998 Venera 14 landing sites, Sov. Astron. Let. vol. 8, No., 4, Jul.-Aug. 1982, 241-242

999 Lognonné, P., W.T. Pike (2015). Planetary seismometry, in Extraterrestrial Seismology, ed. by V.C.H.
1000 Tong, R. Garcia, Cambridge University Press, Cambridge, pp. 36–48. Chap. 3.
1001 doi:10.1017/CBO9781107300668.006

1002 Lognonné, P., and 180 co-authors, SEIS: The Seismic Experiment for Internal Structure of InSight, Space
1003 Science Reviews, submitted

1004 Lorenz, R.D., Kedar, S., Murdoch, N., Lognonné, P., Kawamura, T., Mimoun, D., Banerdt, W.B. (2015).
1005 Seismometer Detection of Dust Devil Vortices by Ground Tilt., Bull. Seis. Soc. Am., vol. 105, No. 6, 3015-
1006 3023, doi: 10.1785/0120150133

1007 Malin, M.C., Edgett, K.S., Posioolova, L.V., McColley, S.M., Noe Dobrea, E.Z. (2006), Present-Day impact
1008 cratering Rate and Contemporary Gully Activity on Mars, Science, vol. 314, 1573-1577,
1009 10.1126/science.1135156

1010 Morschhauser, A., Lesur, V., Grott, M. (2014) A spherical harmonic model of the lithospheric magnetic
1011 field of Mars, J. Geophys. Res. Planets, vol. 119, doi:10.1002/2013JE004555

1012 Nakamura, Y. (2003) New identification of deep moonquakes in the Apollo lounar seismic data, Phys.
1013 Earth Planet. Int., vol. 139, 197-205, doi:10.1016/j.pepi.2003.07.017

1014 Nakamura, Y. (2005) farside deep moonquakes and deep interior of the Moon, J. Geophys. Res., vol. 110,
1015 E01001, doi:10.1029/2004JE002332

1016 Neukum, G., Jaumann, R., Hoffmann, H., Hauber, E., Head, J.W., Basilevsky, A.T., Ivanov, B.A., Werner,
1017 S.C., van Gasselt, S., Murray, J.B., McCord, T., & the HRSC Co-Investigator Team(2004) recent and episod-
1018 ic volcanic and glacial activity on Mars revealed by the high resoltion stereo camera, Nature, vol. 432,
1019 971-979

1020 Oberst, J. (1987). Unusually high stress drops associated with shallow moonquakes, J. Geophys. Res., vol.
1021 92, 1397-1405

1022 Panning, M.P., Lognonné, P., Banerdt, W.B., Garcia, R., golombek, M., Kedar, S., Knapmeyer-Endrun, B.,
1023 Mocuet, A., Teanby, N.A., Tromp, J., Weber, R., Beucler, E., Blanchette-Guertin, J.-F., Bozdağ, E., Drilleau,
1024 M., Gudkova, T., Hempel, S., Khan, A., Lekić, V., Murdoch, N., Plesa, A.-C., Rivoldini, A., Schmerr, N., Rua,
1025 Y., Verhoeven, O., Gao, C., Christensen, U., Clinton, J., Dehant, V., Giardini, D., Mimoun, D., Pike, W.T.,
1026 Smrekar, S., Wiectorek, M., Knapmeyer, M., Wookey, J. (2017), Planned products of the Mars structure
1027 service for the InSight mission to Mars, Space Sci. Rev., vol. 211, 611-650, doi:10.1007/s11214-016-0317-
1028 5

1029 Panning, M.P., Beucler, E., Drilleau, M., Mocwuet, A., Lognonné, P, Banerdt, W.B. (2015) Verifying single-
1030 station seismic approaches using Earth-based data: preparation for data return from the InSight mission
1031 to Mars, Iarus, vol. 248, 230-242, doi:10.1016/j.icarus.2014.10.035

1032 Phillips, R.J. (1991). Expected rates of Marsquakes, in: Scientific Rationale and Requirements for a Global
1033 Seismic Network on mars, LPI Tech Rep. 91-02 LPI/TR-91-02, pp. 35-38, Lunar and Planet. Inst. Houston,
1034 Texas

1035 Plesa A.- C., Knapmeyer, M., Golombek, M.P., Breuer, D., Grott, M., Kawamura, T., Lognonné, P., Tosi,
1036 N., and Weber, R. (2018), Present-day Mars' Seismicity Predicted from 3-D Thermal Evolution Models of
1037 Interior Dynamics, Geophys. Res. Lett., 45, doi:10.1002/2017GL076124.

1038 Reasenberg, P. (1985). Second-Order moment of central California seismicity, J. Geophys. Res., vol. 90,
1039 No. B7, 5479-5495

1040 Schulte, S.M.; Mooney, W.D. (2005) An updated global earthquake catalog for stable continental regions:
1041 reassessing the correlation with ancient rifts; Geophys. J. Int., vol. 161, 707-721

1042 Schulz, R.A., Okubo, C.H., Wilkins, S.J. (2006) Displacement-length scaling relations for faults on the ter-
1043 restrial planets, J. Struct. Geol. vol. 28, 2182-2193, doi: 10.1016/j.jsg.2006.03.034

1044 Schulz, R.A., Soliva, R., Okubo, C.H., Mège, D. (2010), Fault populations, in: Watters, T.R., Schulz, R.A.
1045 (eds.), Planetary Tectonics, Cambridge University Press, 457-510

1046 Siddiqi, A.A. (2002), Deep Space Chronicle, NASA SP-2002-4524, Monographs in Aerospace History, No.
1047 24, 256 pages

1048 Taylor, J., Teanby, N., Wookey, J. (2013). Estimates of seismic activity in the Cerberus Fossae region on
1049 Mars, vol. 118, 2570-2581, doi:10.1002/2013JE004469

1050 Teanby, N.A., Wookey, J. (2011), Seismic detection of meteorite impacts on Mars, Phys. Earth Planet.
1051 Int., vol. 186, 70-80, doi:10.1016/j.pepi.2011.03.004

1052 Toksöz, M. Nafi (1979). Planetary Seismology and Interiors, Rev. Geoph. Space Phys., vol. 17, No. 7, 1641-
1053 1655

1054 Vere-Jones, D. (1976). A branching model for crack propagation, Pure Appl. Geophys., vol. 114, 711-725

1055 Vere-Jones, D., Robinson, R., Yang., W. (2001). Remarks on the accelerated moment release model:
1056 problems of model formulation, simulation and estimation; GJI, vol. 144, 517-531

1057 Vostreys, R.W. (1980), Data User's Note - Apollo Seismological Investigations, NSSDC/WDC-A-R&S 80-11,
1058 NASA-TM-82280, 27 pages, available online:
1059 https://ntrs.nasa.gov/archive/nasa/casi.ntrs.nasa.gov/19810009447.pdf, last accessed 19.02.2018

1060 Wason, H.R., Das, R., Sharma, M.L. (2012) Magnitude conversion problem using general orthogonal re-
1061 gression, Geophys. J. Int., vol. 190, 1091-1096, doi: 10.1111/j.1365-246X.2012.05520.x

1062 Weber, R.C.; Bills, B.G., Johnson, C.L. (2010) A simple physical model for deep moonquake occurrence
1063 times, Phys. Earth Planet. Int., vol. 182, 152-160, doi:10.1016/j.pepi.2010.07.009

1064 Weisstein, Eric W. (undated). Gamma Function, MathWorld--A Wolfram Web Resource.
1065 http://mathworld.wolfram.com/GammaFunction.html, last accessed 26. October 2017

1066 Wyrick, D. Y., Morris, A.P., Ferrill, D.A. (2018), Normal fault gropth in analog mdoels and on Mars, Icarus,
1067 vol. 212, 559-567, doi:10.1016/j.icarus.2011.01.011

1068 Young, J.B.; Presgrave, B.W.; Aichele, H.; Wiens, D.A.; Flinn, E.A. (1996) The Flinn-Engdahl Regionalisation
1069 Scheme: the 1995 revision; Phys. Earth Planet. Int., vol. 96, 223-297

1070 Zhuang, J., D. Harte, M.J. Werner, S. Hainzl, and S. Zhou (2012), Basic models of seismicity: temporal
1071 models, Community Online Resource for Statistical Seismicity Analysis, doi:10.5078/corssa-79905851.
1072 Version 1.0, issued 14. Aug. 2012. Available at http://www.corssa.org

1073 Zhuang, J. & S. Touati (2015), Stochastic simulation of earthquake catalogs, Community Online Resource
1074 for Statistical Seismicity Analysis, doi:10.5078/corssa-43806322. Version 1.0, issued 19. March 2015,
1075 Available at http://www.corssa.org

1076 Zuber, M.T., Solomon, S.C., Phillips, R.J., Smith, D.E., Tyler, G.L., Aharonson, O., Balmino, G., Banerdt,
1077 W.B., Head, J.W., Johnson, C.L., Lemoine, F.G., McGovern, P.J., Neumann, G.A., Rowlands, D.G., Zhong, S.
1078 (2000) Internal structure and early thermal evolution of Mars from Mars Global Surveyor Topography
1079 and Gravity, Science, vol. 287, 1788-1793

1080

DLR Institute for Planetary Research
Rutherfordstr. 2
12489 Berlin
Germany
(MK, ACP)

Max Planck Institute for Solar System Research
Justus-von-Liebig-Weg 3
37077 Göttingen
Germany
(BKE)

Jet Propulsion Laboratory
California Institute of Technology
Pasadena, CA 91109
USA
(MPG, SK)

NASA Marshall Space Flight Center
320 Sparkman Drive
Huntsville
AL 35805
USA
(RCW)

Swiss Seismological Service
ETH Zürich
Sonneggstrasse 5
8092 Zürich
Switzerland
(MB, JFC, SS)

AWE Blacknest

Brimpton

Reading

Berkshire RG7 4RS

UK

(JS)

School of Earth Sciences

University of Bristol

Wills Memorial Building

Queens Road

Bristol BS8 1RJ

UK

(NAT)

Institute de Physique du Globe de Paris (IPGP)

Bât. Lamarck

35 rue Hélène Brion

75205 Paris CEDEX 13

France

(TK, CP, PL)

Tables

Table 1 Annual seismic moment rate of Earth, Moon, and Mars.

Planet	Reference	Method	Annual Rate [Nm/yr]	Annual Rate [Equiv. Mag. per yr]
Earth	GCMT	observed quakes, 1976-2018	7.61×10^{21}	8.5
Moon	Oberst, 1987	observed HFT quakes	7.27×10^{14}	3.8
Mars	Anderson et al., 1977	Viking non-observation of quakes	$Moon \leq Mars < Earth$	
	Goins & Lazarewicz, 1979	Viking non-observaation of quakes	$< Earth$	
	Phillips, 1991	1D lithospheric cooling model	4.8×10^{18}	6.4
	Golombek et al., 1992	Observed surface fault-ing	10^{18}	5.9

	Golombek, 2002	Observed surface faulting	10^{18} to 10^{19}	5.9 to 6.6
	Knapmeyer et al., 2006	1D lithospheric cooling model, weak, medium, and strong scenario	3.42×10^{16} 5.99×10^{17} 4.78×10^{18}	4.96 5.8 6.4
	Taylor et al., 2013	Observed surface faulting	$> 5.5 \times 10^{16}$	>5.09
	Plesa et al., 2018	3D whole-mantle thermal evolution model	5.7×10^{16} to 3.9×10^{19}	5.1 to 7

1132 Equivalent magnitudes are moment magnitudes computed according to eq. 1 assuming that the en-
1133 tire moment release of one year is put into a single event.

1134

1135 **Table 2 Quality levels used to categorize Goldstone seismograms**

Category	Definition	Event count
A	prominent arrivals of various body and surface wave phases	38
B	P arrival and Rayleigh waves clearly above noise level	19
C	P arrival and Rayleigh waves barely above noise level	13
D	Only body waves visible	4
E	Only surface waves visible	60
F	Invisible	170

1136

1137

1138 **Table 3 Annual moment rate estimations for different settings on Earth**

Subset (No. of events)	$\boldsymbol{\Sigma}$	$\boldsymbol{KS_{10}}$	$\boldsymbol{NLVR}$	**Units**
All events (49178)	76.1	54.9	33.6	10^{20} Nm/yr
	8.52	8.43	8.28	Magnitude
Subduction Zones (32855)	66.9	54.9	33.6	10^{20} Nm/yr
	8.48	8.43	8.28	Magnitude
Mid-Ocean Ridges (7783)	1.63	1.11	1.07	10^{20} Nm/yr
	7.41	7.3	7.29	Magnitude
Subduction Zones, $z \geq 100\ km$ (7297)	7.38	6.1	2.49	10^{20} Nm/yr
	7.85	7.79	7.53	Magnitude
Subduction Zones, $z < 100\ km$ (26003)	59.8	52.1	33.6	10^{20} Nm/yr
	8.45	8.41	8.28	Magnitude
Stable Continental Regions, historic events (226)	0.0571	0.0405	0.0415	10^{20} Nm/yr
	6.44	6.34	6.35	Magnitude
Stable Continental Regions, instrumental	0.101	0.124	0.17	10^{20} Nm/yr
	6.6	6.66	6.75	Magnitude

events (879)				

Annual moment rate estimations for several subsets of the GCMT catalog from 1976 to 2018, for historically witnessed events in stable continental regions between 1500 and 1949, and finally instrumentally recorded events in stable continental regions, between 1950 and 2003. The first column is the estimate resulting from summing up all events in the subset, the second is the KS for the 10 strongest events, and the third column is the NLVR estimator resulting from the single strongest event. Each estimate is given in Newton meters per year and as moment magnitude of a single event releasing the same amount of Newton meters.

Table 4 Annual moment rate models for Mars

Model	$\dot{M}_S$ [Nm/yr]	M_{Max} [Nm]	M_C [Nm]	$m_S - m_C$
StrongFew	4.78×10^{18}	3.36×10^{20}	1.31×10^{20}	-0.96
StrongMany	4.78×10^{18}	3.42×10^{16}	1.33×10^{16}	+1.70
Medium	5.99×10^{17}	2.41×10^{18}	9.42×10^{17}	-0.13
WeakMany	3.42×10^{16}	3.42×10^{16}	1.33×10^{16}	+0.27
WeakFew	3.42×10^{16}	3.37×10^{20}	1.32×10^{20}	-2.39

Moment rates, maximum moments, and corresponding corner moments of the end-member seismicity models of Knapmeyer et al., 2006. All models use a slope parameter of $\boldsymbol{\beta = 0.625}$.

1152

Figures

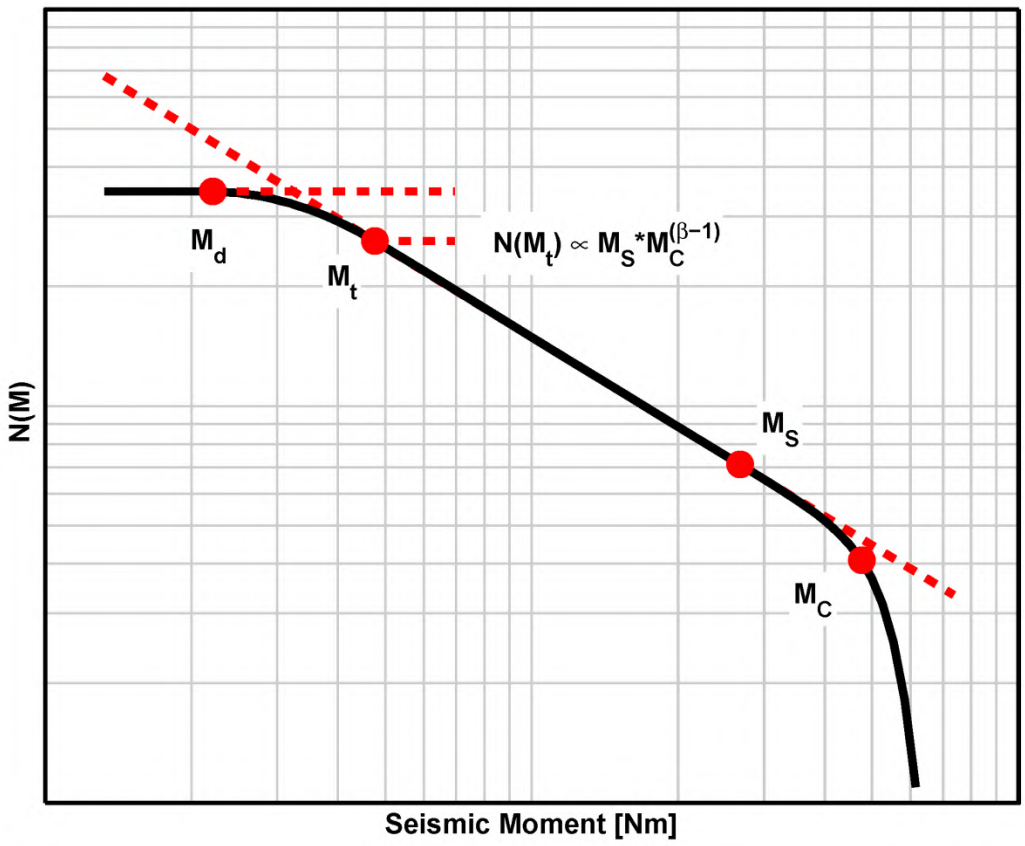

Figure 1 Schematic depiction of the tapered Gutenberg-Richter distribution in survivor form, showing the number N of events exceeding moment M. Bullets mark characteristic moment values: M_d - detection threshold, no event smaller than this is contained in a catalog; M_t - completeness threshold, all events above this are cataloged; M_S - size of an event corresponding to the average moment rate; M_C - corner moment. The corner moment may or may not be larger than M_S. slanted dashed line: prediction according to a Gutenberg-Richter law with the same slope. Horizontal dashed lines: (lower) number of events above completeness threshold M_t, to be used for event rate estimation; (upper) number of events in catalog. Gray: an arbitrary grid to indicate that the graph is drawn in log-log coordinates (at M_C, the tapered distribution is actually below the classical GR distribution by a factor e).

1164

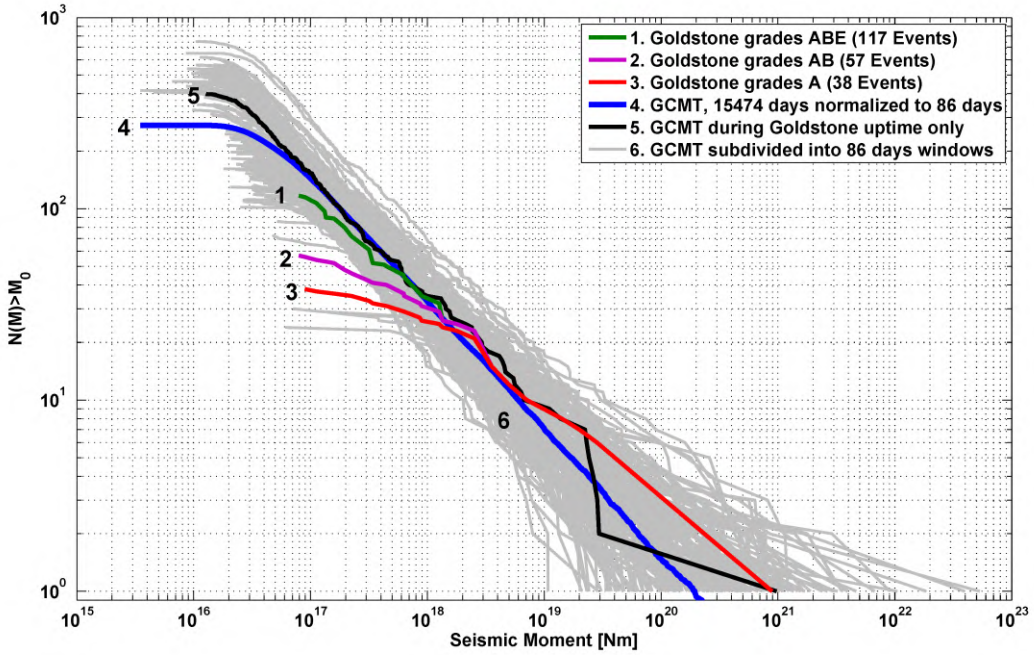

Figure 2 Size-frequency survivor distributions for events detected at Goldstone (in groups containing grade A only, or grades A and B, or grades A, B, and E, as indicated in legend. Note that the ABE line is partially covered by the AB line, which in turn gets covered by the A line), the subset of events listed in the GCMT for the uptime of the Goldstone experiment (labeled 5), the whole GCMT scaled down to a duration of 86 days (labeled 4). The gray curves in the background show distributions for consecutive 86-days time windows (i.e. days 1 to 86, 87 to 173, 174 to 260, ... etc.) throughout the entire GCMT catalog.

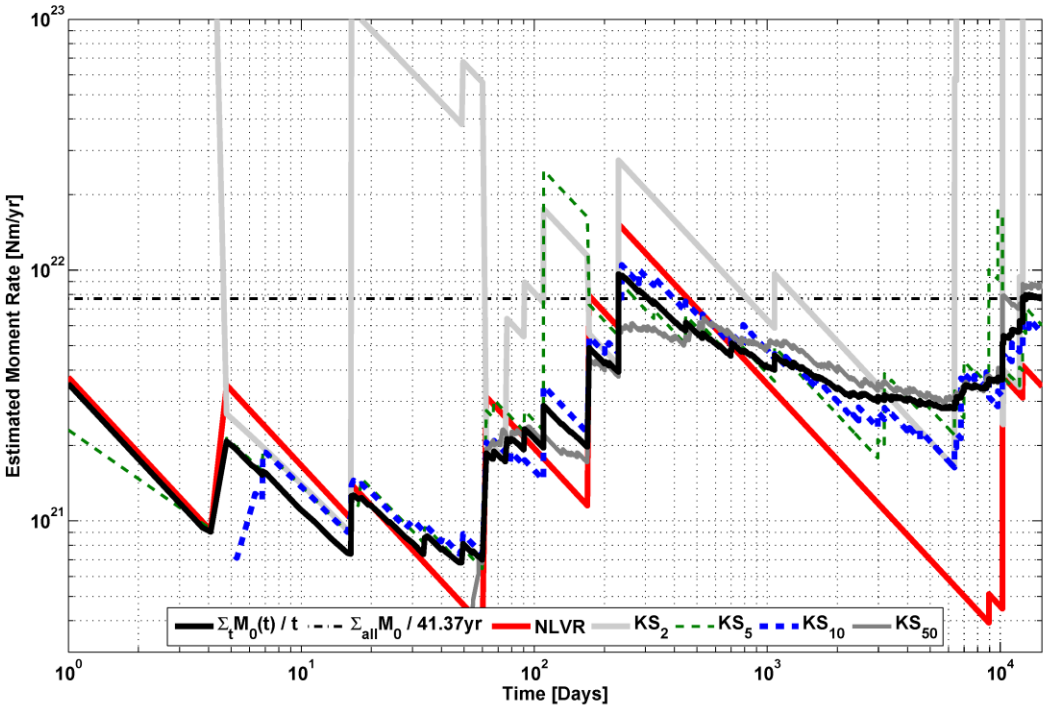

1174

1175 **Figure 3 Evolution in time of moment rate estimations for Earth. The bold black curve is based on summation of all events**

1176 **in the GCMT catalog. The horizontal line marks its value at the end of the cataloged time (01.01.1977 to 18.05.2018). Other**

1177 **lines show time series for the $NLVR$ and KS_k estimators according to the legend.**

1178

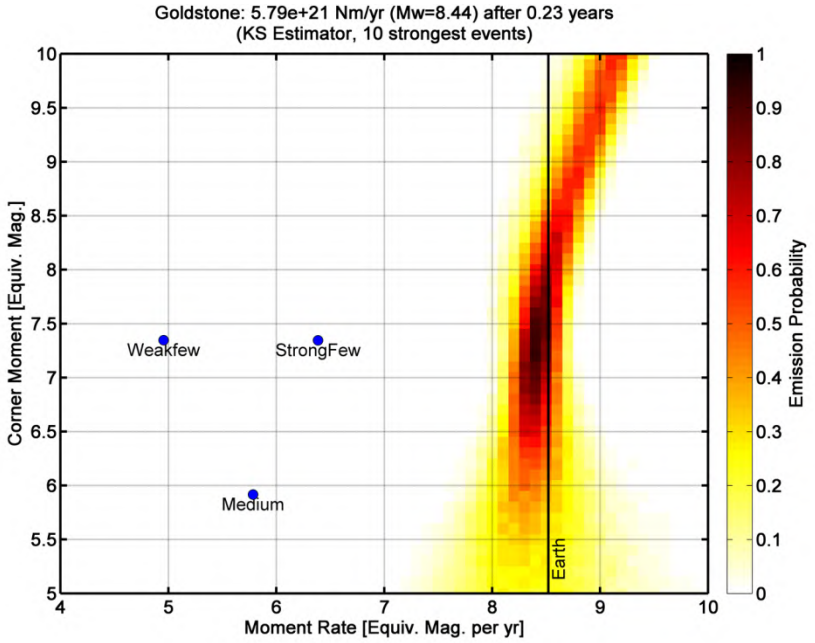

Figure 4 KS_{10} emission probability for the events detected at Goldstone (grade A events only). Dots mark the moment rates and corner moments of all five Mars seismicity scenarios of Knapmeyer et al. (2006), pixel color encodes the emission probability for matching the target rate within 0.2 magnitudes, as derived from 1000 simulated catalogs per pixel. Coordinate axes are labeled in terms of equivalent moment magnitudes. The vertical black line to the right gives the moment rates of the Earth, as listed in Table 1.

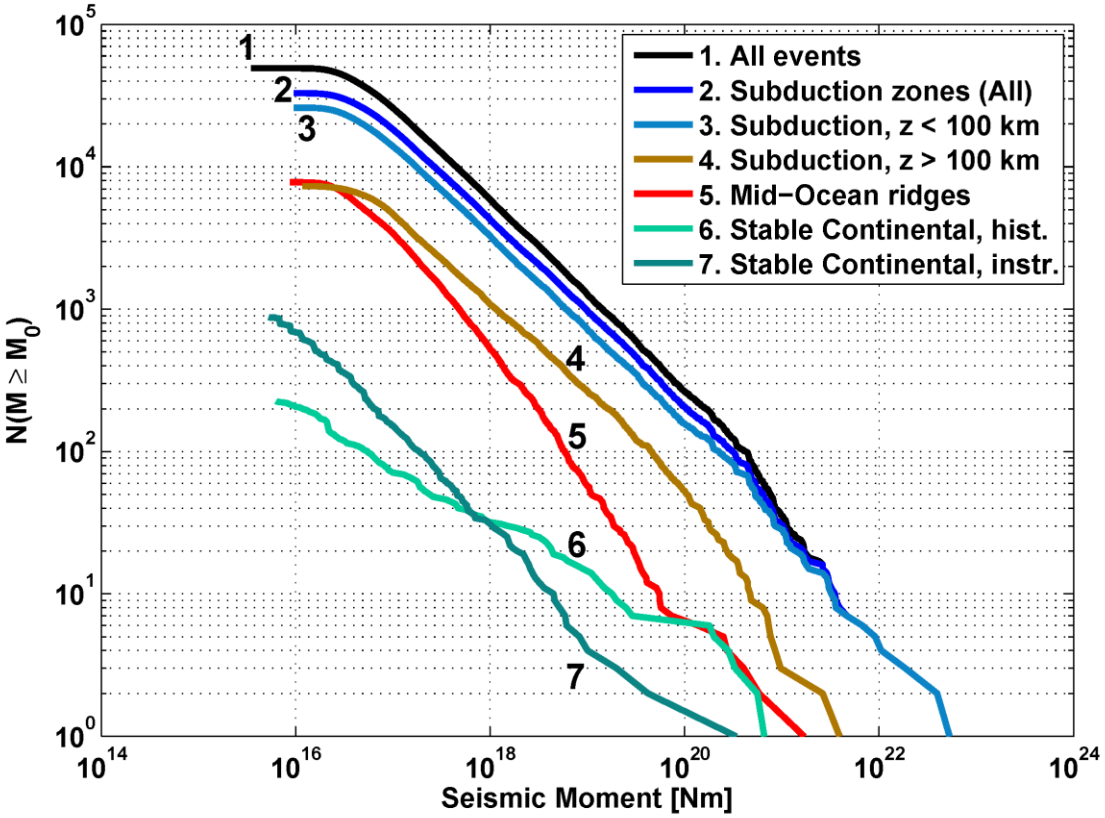

Figure 5 Size-Frequency distributions of several subsets of the GCMT catalog and of the Stable Continental Regions catalog. Subduction zones and mid-ocean ridges are identified by using the Flinn-Engdahl regionalization scheme, and subduction zone events are further subdivided into events occurring above and below 100 km depth. The complete GCMT catalog is shown for comparison. For the Stable Continental Regions catalog, the distributions of events from 1500 to 1949 and from 1950 to 2003 are shown separately.

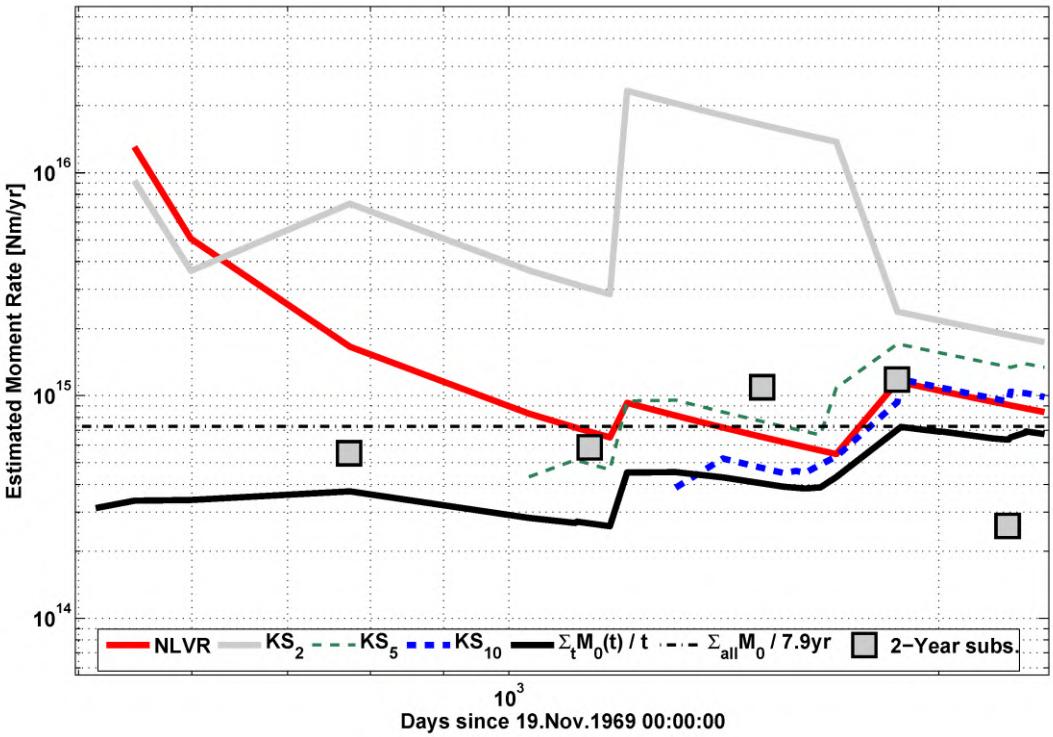

Figure 6 Evolution in time of moment rate estimations for shallow moonquakes. Lines denote estimator output as in Figure 3, applied to the seismic moments of Oberst (1987). Squares denote the sum of two calendar years of registrations, plotted at the relative time of the first of January of the first year, intervals used are 1972-1973, 1974-1975, 1976-1977, 1973-1974, and 1975-1976.

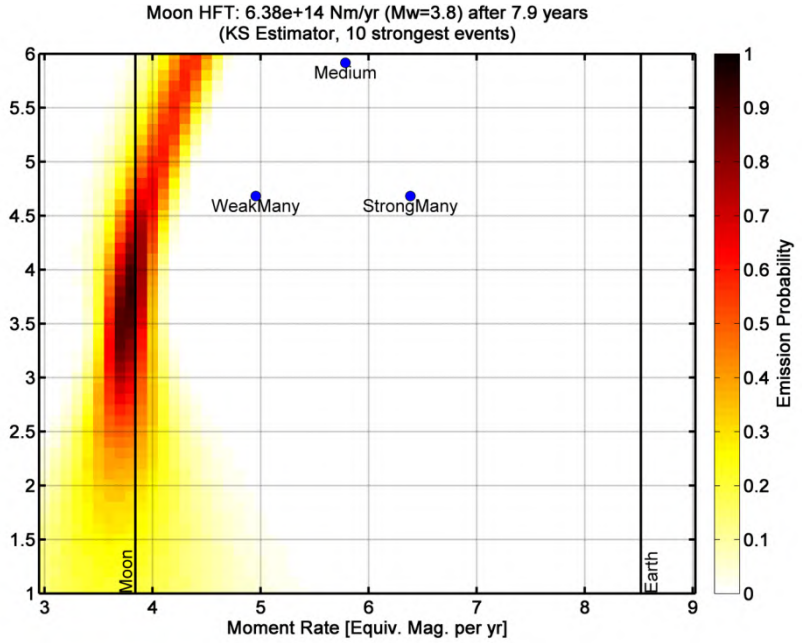

Figure 7 KS_{10} emission probability for shallow moonquakes. Dots mark the moment rates and corner moments of Mars seismicity scenarios of Knapmeyer et al. (2006) for comparison, pixel color encodes the emission probability for matching the target rate within 0.2 magnitudes, as derived from 1000 simulated catalogs per pixel. Coordinate axes are labeled in terms of equivalent moment magnitudes. The two vertical black lines give the moment rates of Moon and Earth, as listed in Table 1.

1207

1208

1209

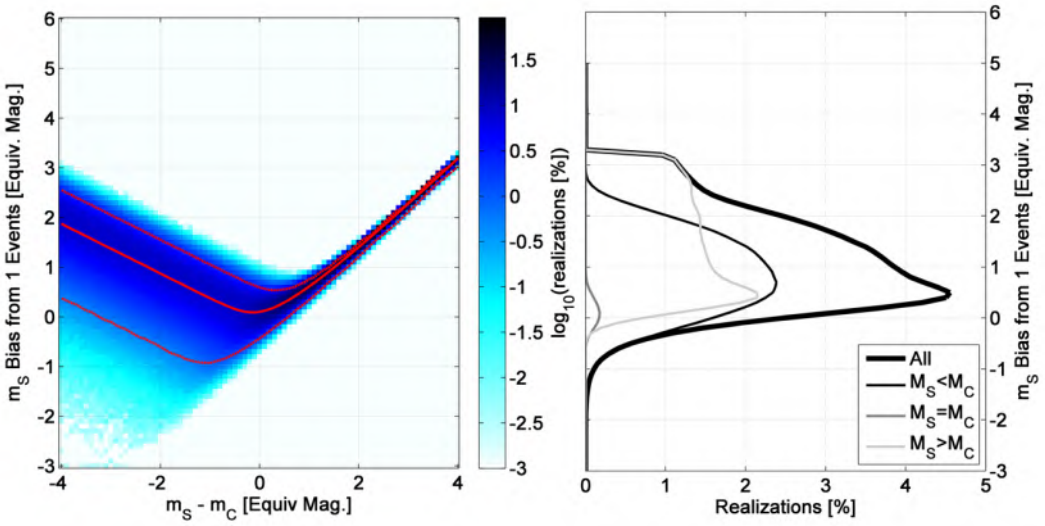

Figure 8 NLVR Cumulative moment bias for synthetic catalogs, using $\beta = 2/3$ in both generation and interpretation of catalogs. Left: Histograms resulting from the 8108910 synthetic catalogs generated for the cumulative moment to corner moment ratio indicated on the x-axis, shading encodes the logarithm of the percentage of realizations in each moment rate bias bin of width 0.1. Positive values on the y-axis indicate underestimation. Solid line: median, dashed lines: upper and lower boundary of the 95%-quantile centered around the median. Right: marginal distribution density resulting from row-wise integration of the figure to the left. Thick line: all catalogs, other: relation between moment rate M_S and corner moment M_C as indicated in legend.

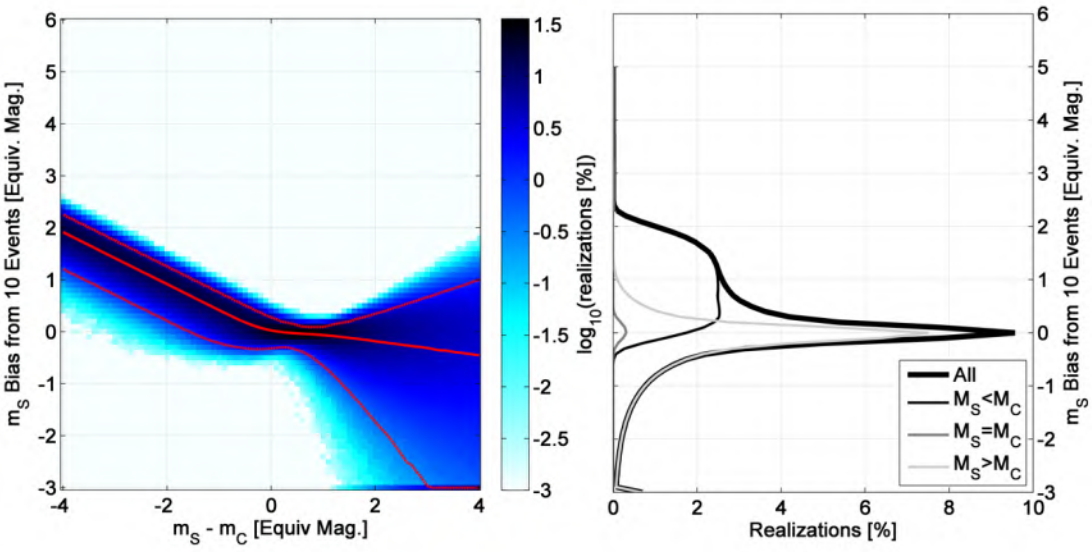

Figure 9 KS_{10} Cumulative moment bias for synthetic catalogs, using $\beta = 2/3$ in both generation and interpretation of catalogs. See Figure 8 for a description of graph elements.

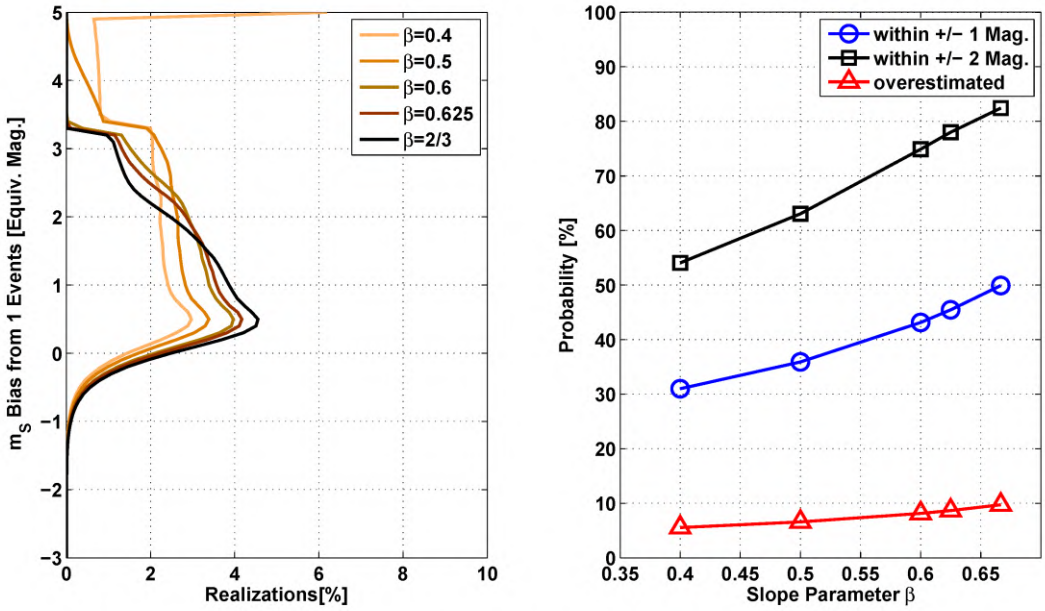

Figure 10 NLVR estimator marginal distribution densities for different slope parameters. Left: the marginal distribution densities for all catalogs (corresponding to the grey curve in Figure 8). Each curve represents approx. 8 million evaluated catalogs. Right: percentage of estimations that are within ± 1 (blue) or ± 2 magnitudes (black) from the true moment rate, and the fraction of overestimated moment rates (red).

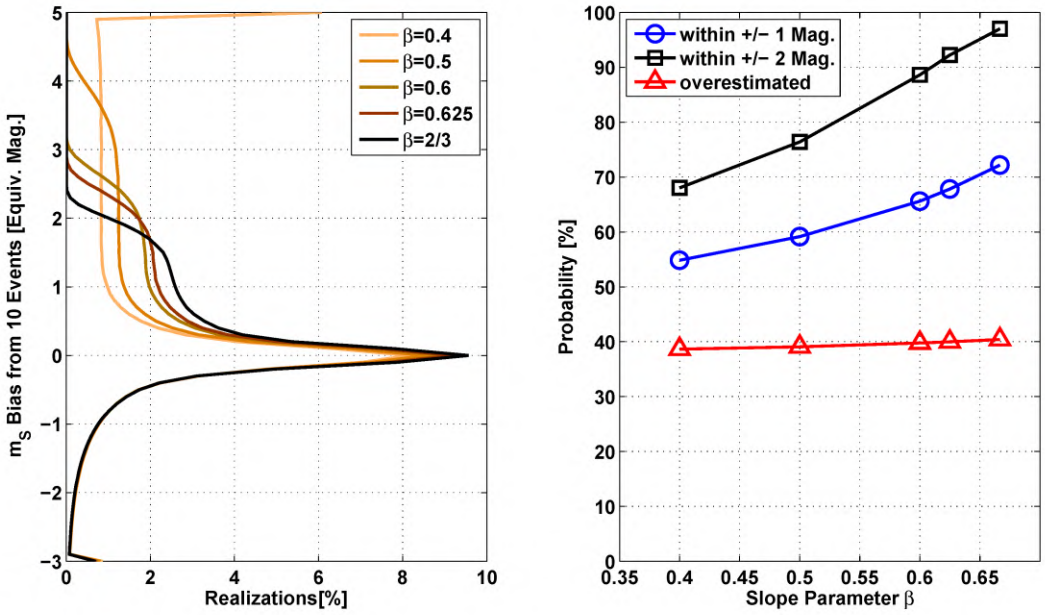

Figure 11 KS_{10} estimator marginal distribution densities for different slope parameters. See Figure 10 for a plot description.

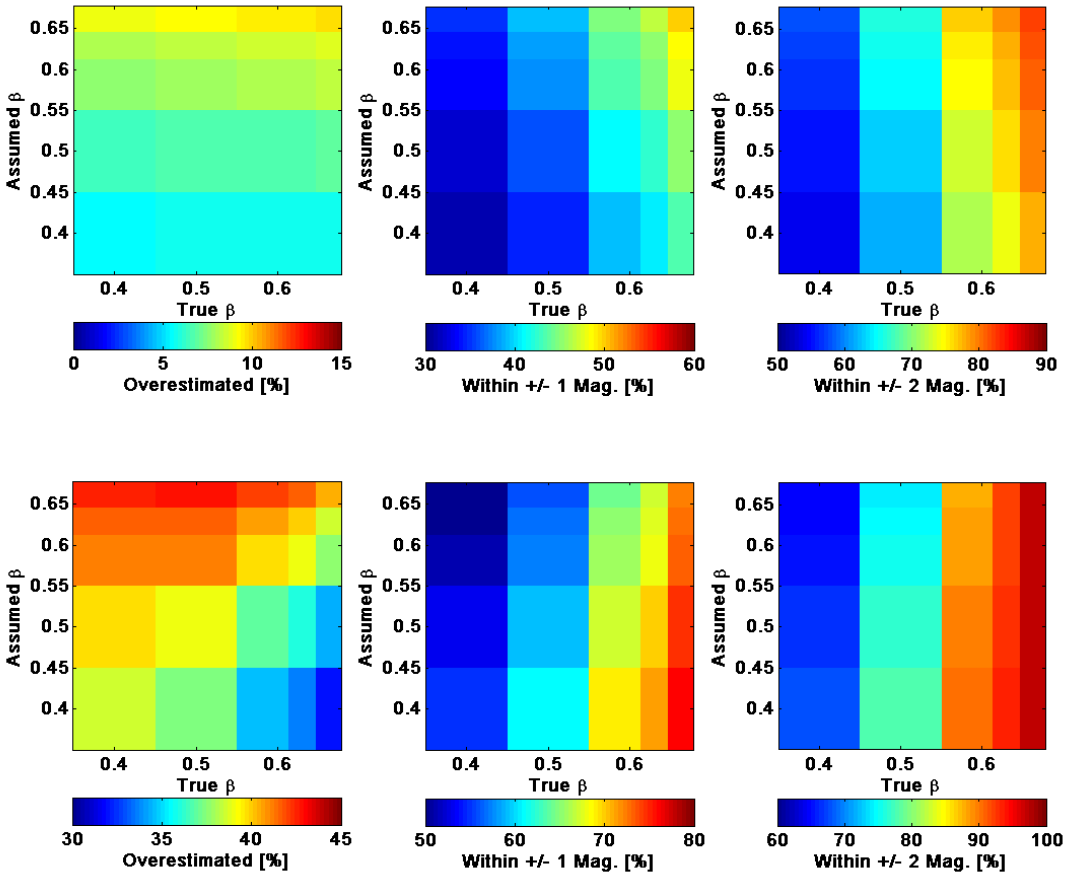

Figure 12 Distribution width parameters for NLVR (top row) and KS_{10} (bottom row) estimators. Each uniformly colored patch indicates the width parameter of distribution densities as shown in Figure 10 and Figure 11. True slope and slope assumed during catalog evaluation were taken from $\{0.4, 0.5, 0.6, 0.625, 2/3\}$ to form a square matrix of test cases. From left to right: percentage of cases with overestimated moment rate, percentage of moment rate estimations within ± 1 magnitude of true value, or within ± 2 magnitudes, respectively. Panels in the same subplot column share the same color range width, although the absolute values differ.

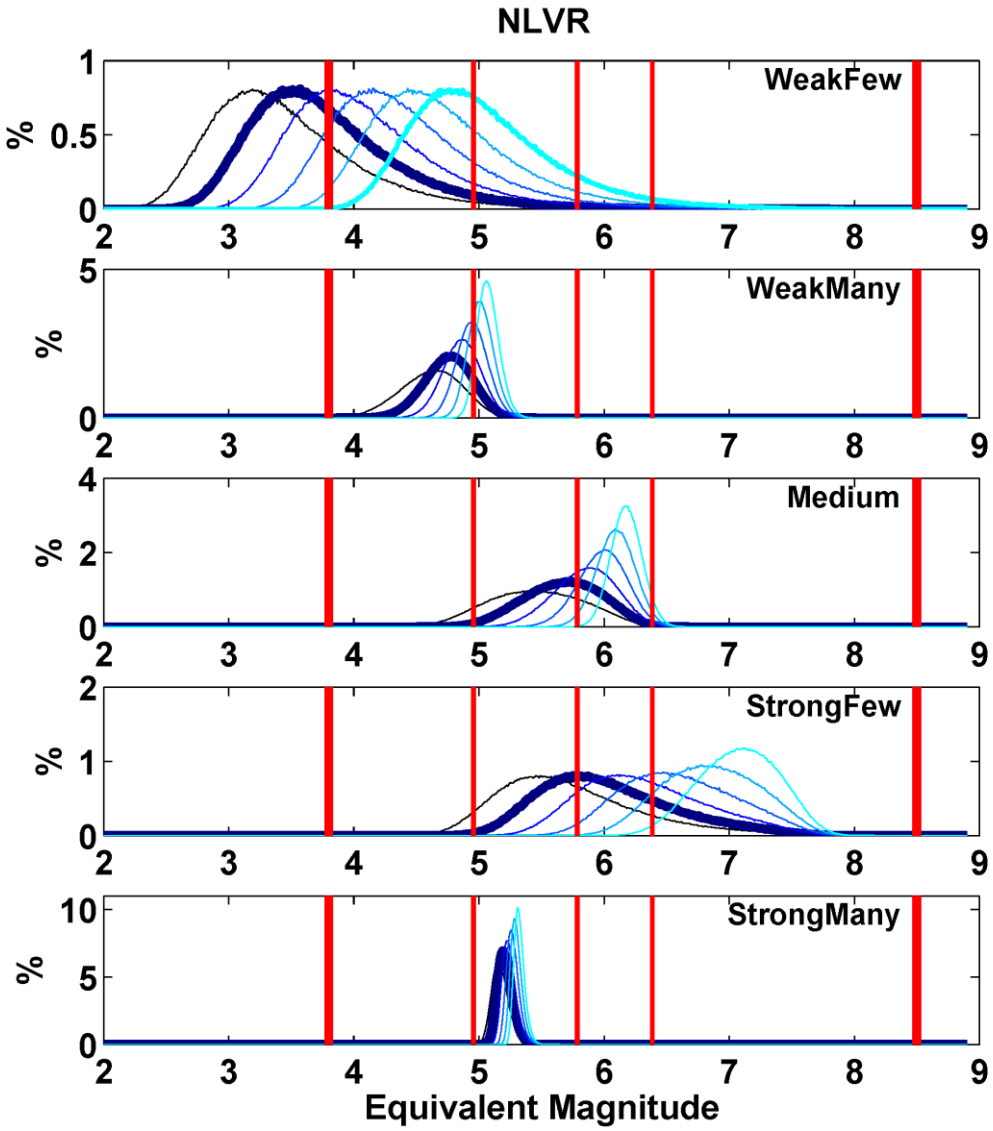

Figure 13 Distribution of NLVR estimators for Mars-specific seismicity models of Knapmeyer et al. (2006) and registration times of 1, 2, 4, 8, 16, and 32 years (envelopes of histograms with bin width 0.01 magnitudes, scaled to percents). Panels from top to bottom show the distributions for seismicity models as indicated in the panel. Note the different y axis ranges.. The seismic moment rate is given as the moment magnitude of a single event that releases the entire moment in one event (the axis range corresponds to $1.3 \times 10^{12} \ldots 4 \times 10^{22}\ Nm$). Darker hues correspond to shorter registration times, the two-year case also uses a thicker line. Vertical lines from left to right denote moment rates (as equivalent magnitudes) for the Moon, both *Weak* scenarios, *Medium* scenario, both *Strong* scenarios, and Earth .

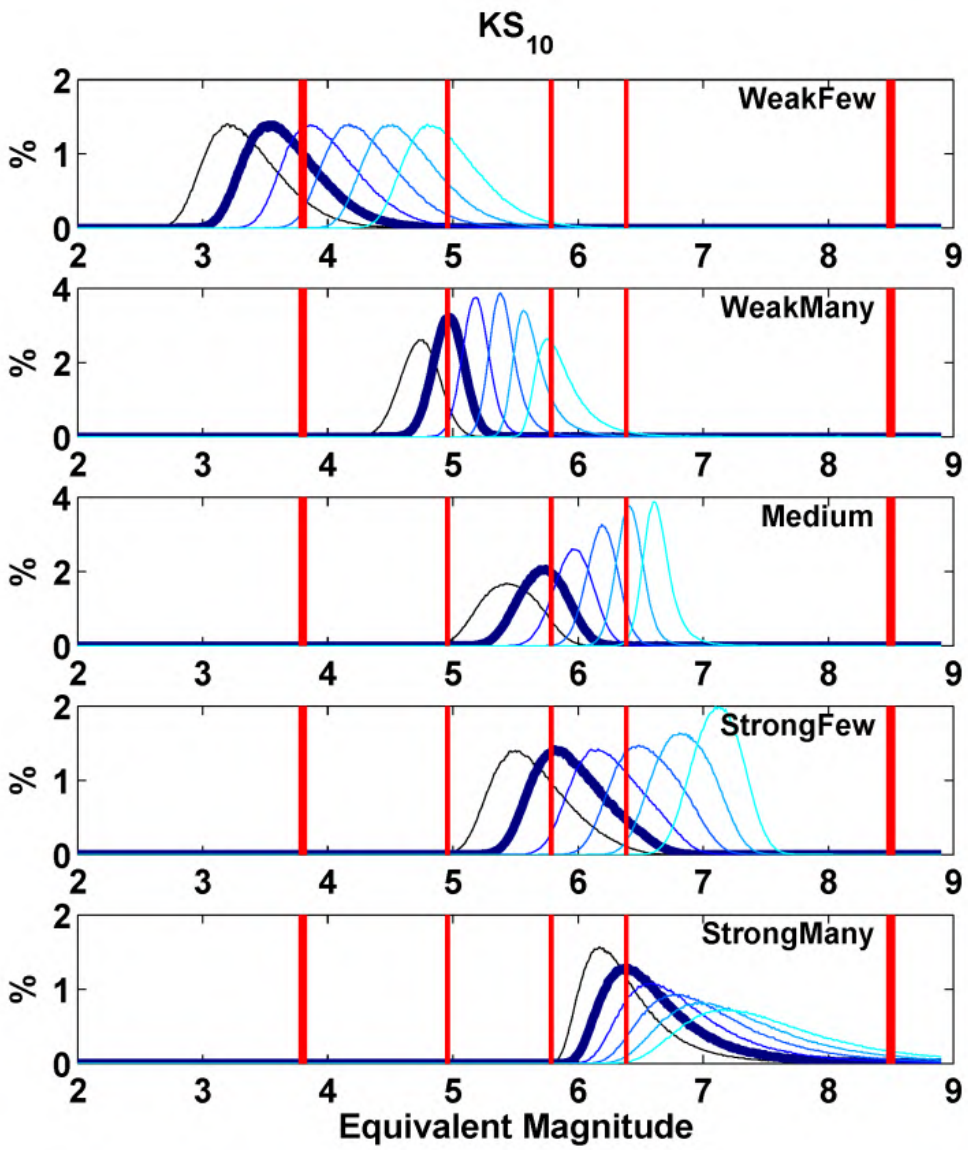

1252

1253 **Figure 14 As Figure 13, but for the KS_{10} estimator.**

1254

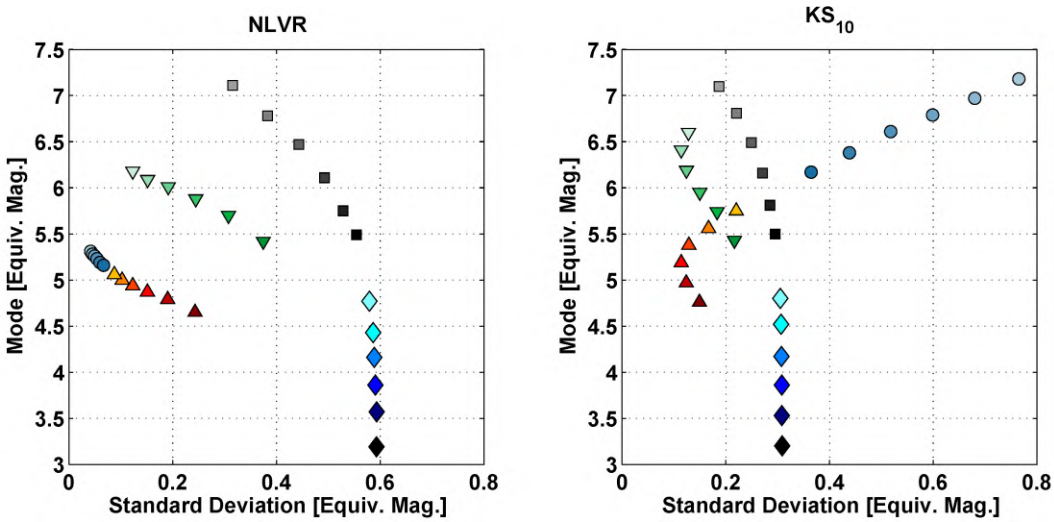

1255

1256 **Figure 15 Standard deviations and modes of the distribution densities shown in Figure 13 and Figure 14. Brigthter shades**

1257 **indicate longer registration times, symbols encode the end member models of Knapmeyer et al. (2006). Diamonds: *WeakFew*,**

1258 **Upward triangles: *WeakMany* Downward triangles: *Medium*, Circles: *StrongMany*, Squares: *StrongFew***

1259

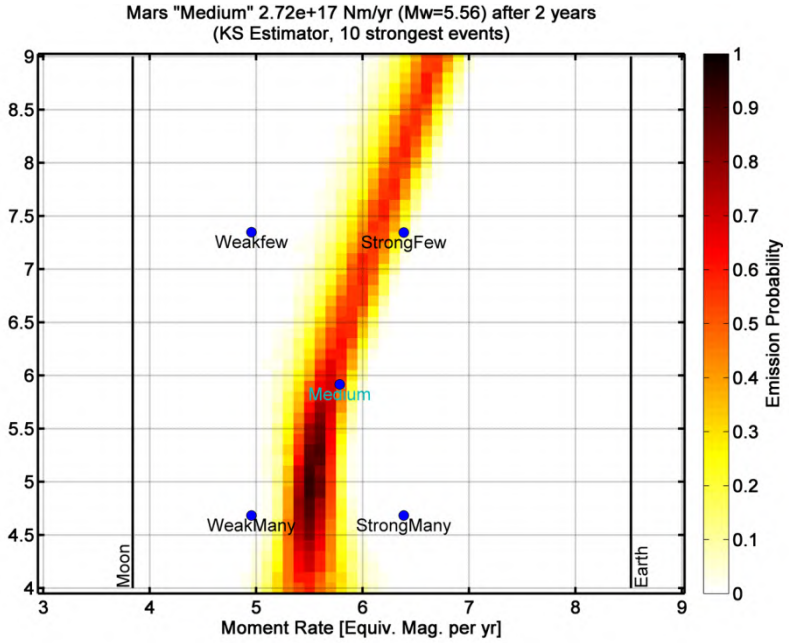

Figure 16 KS_{10} emission probability for a synthetic Mars *Medium* catalog. Dots mark the moment rates and corner moments of Mars seismicity scenarios of Knapmeyer et al. (2006) for comparison, pixel color encodes the emission probability for matching the target rate within 0.2 magnitudes, as derived from 1000 simulated catalogs per pixel. Coordinate axes are labeled in terms of equivalent moment magnitudes. The two vertical black lines give the moment rates of Moon and Earth, as listed in Table 1.

1267

1268

Appendix

Flinn-Engdahl zones

In the analysis of the GCMT catalog, we used the Flinn-Engdahl zonation scheme, in the revision of Young et al. (1995), to classify events as belonging to either subduction zones or mid-ocean ridges.

We consider as mid-ocean ridge events all events in zones

143 149 150 401 401 402 403 404 405 406 408 409 410 411 413 419 424 425 426 427 428 429 433 634 635 636 637 638 641 648 681 682 683 688 691 692 693 694 698 699 727 729 735 737 738 739 753 754

We consider as subduction zone event all events in zones

1 2 4 5 6 7 9 10 12 13 14 57 58 59 60 61 66 68 69 70 71 73 74 76 77 78 91 92 95 99 102 103 105 106 107 108 109 110 111 112 113 114 115 116 117 118 119 120 121 122 123 124 125 127 127 128 129 130 131 132 134 135 136 136 137 138 139 141 144 145 153 159 160 169 171 171 172 173 174 175 176 176 177 178 180 181 182 183 184 185 188 189 191 192 193 199 200 201 202 206 209 210 211 212 214 215 216 217 218 219 220 221 223 226 227 228 229 231 233 234 236 237 242 244 245 247 248 249 250 255 258 261 262 263 264 265 266 268 269 271 272 273 274 275 276 277 278 279 281 282 283 284 285 286 290 366 367 368 387 388 396 654 657 658 659 660 685 700 701 702 703

We consider as subducting slabs all events in the subduction zones as listed above, and deeper than 100 km.